LARGE-SCALE SEABED DYNAMICS IN OFFSHORE MORPHOLOGY: MODELING HUMAN INTERVENTION

Pieter C. Roos and Suzanne J. M. H. Hulscher
Water Engineering and Management, University of Twente, Enschede, Netherlands

Received 23 October 2002; revised 28 January 2003; accepted 19 February 2003; published 28 June 2003.

[1] We extend the class of simple offshore models that describe large-scale bed evolution in shallow shelf seas. In such seas, shallow water flow interacts with the seabed through bed load and suspended load transport. For arbitrary topographies of small amplitude we derive general bed evolution equations. The initial topographic impulse response (initial sedimentation and erosion patterns around an isolated feature on a flat seabed) provides analytical expressions that provide insight into the inherent instability of the flat seabed, the Coriolis-induced preference for cyclonically oriented features, and bed load transport being a limiting case of suspended load transport. The general evolution equation can be used to describe sandbank formation, known as the result of self-organization. Examples of human intervention at the seabed include applications to a dredged channel and an offshore sandpit. An outlook toward future research is also presented. *Index Terms:* 3210 Mathematical Geophysics: Modeling; 1824 Hydrology: Geomorphology (1625); 1815 Hydrology: Erosion and sedimentation; 1255 Geodesy and gravity: Tides-ocean (4560) 4508 Oceanography: Physical: Coriolis effects; *Keywords:* morphodynamics, offshore, morphology, sandbanks

Citation: Roos P. C., and S. J. M. H. Hulscher, Large-scale seabed dynamics in offshore morphology: Modeling human intervention, *Rev. Geophys., 41*(2), 1010, doi:10.1029/2002RG000120, 2003.

1. INTRODUCTION

[2] The North Sea is a tidally dominated shelf sea in which complex morphodynamic processes take place. This can be seen from the variety of rhythmic patterns on different length scales that cover the North Sea bed [*Knaapen et al.*, 2001a; *Hulscher and Van den Brink*, 2001]. In addition to this natural behavior, man also uses the seabed in various ways, for example, navigation dredging, pipeline construction, and sand mining. The long-term fate of such morphological intervention is unclear, as it may interfere with natural seabed dynamics that, despite considerable advances (see, e.g., the review by *Blondeaux* [2001]), are not yet fully understood.

[3] We focus on an offshore tidally dominated environment and restrict our study to large-scale seabed dynamics, i.e., on horizontal length scales of the order of kilometers. Our goal is to derive evolution equations for arbitrary seabed topographies, such as sandbank patterns, isolated sandbanks, dredged channels, or sandpits. This can be done by studying the topographic impulse response: the initial bed response, i.e., initial sedimentation and erosion (ISE) patterns, induced by an isolated topographic feature on an otherwise flat seabed (Figure 1). The response to an arbitrary topography, which can be seen as a superposition of such features, follows from the convolution integral of impulse response and topography. The impulse response, effectively containing all information of a linear system, turns out to provide a link between studies into natural seabed dynamics (sandbank formation) and studies into the morphodynamic impact of human intervention (dredged channel, offshore sandpit, etc.). We focus on the class of linear, process-based, offshore models with a two-dimensional horizontal flow model in combination with a sediment transport mechanism.

[4] Past research within this class of models focused mainly on the formation of tidal sandbanks, with a wavelength of several kilometers, a height of up to 80% of the water depth, and a slightly cyclonic crest orientation with respect to the tidal current [*Dyer and Huntley*, 1999]. *Huthnance* [1982a] was the first to explain their formation as a morphodynamic instability of a flat seabed subject to tidal flow. Friction-topography and Coriolis-topography interactions [*Zimmerman*, 1981; *Loder*, 1980; *Robinson*, 1983; *Pattiaratchi and Collins*, 1987] over a wavy bed trigger a secondary flow, thus causing (bed load) sediment transport, which results in bank growth. Subsequent analyses have further elaborated on this idea, considering more realistic flow conditions and alternative transport mechanisms [*De Vriend*,

8755-1209/03/2002RG000120*$15.00* doi:10.1029/2002RG000120

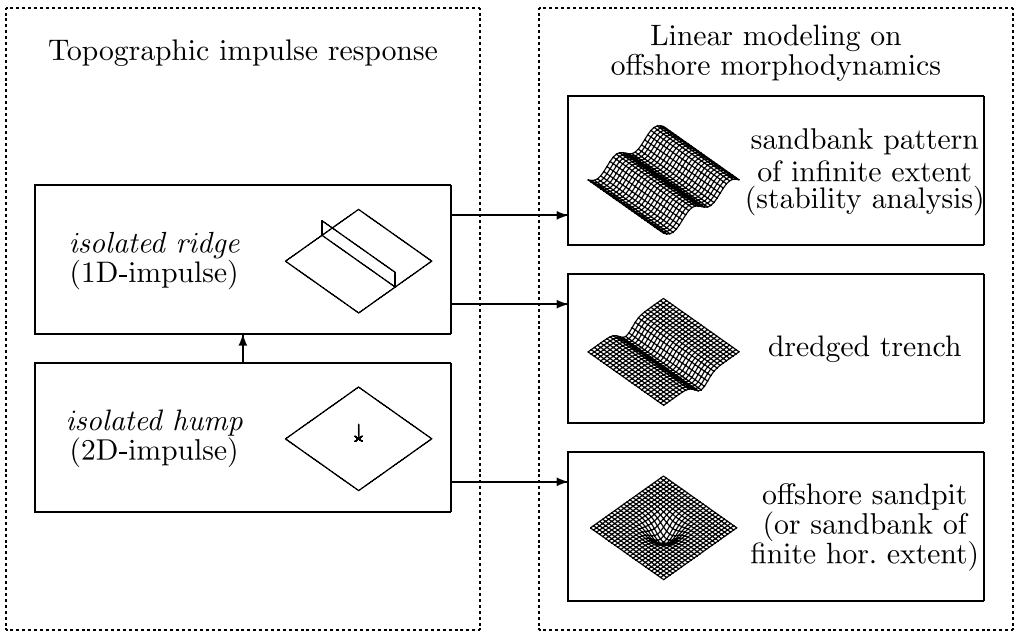

Figure 1. Schematic representation of linear modeling of offshore morphodynamics and its relation to the topographic impulse response. The arrows show how the various items can be derived from the impulse responses and how the two impulse responses relate to each other.

1990; *Hulscher et al.*, 1993]. *Huthnance* [1982a] described the evolution of wavy bed patterns of infinite spatial extent. In a companion paper, *Huthnance* [1982b] described the evolution of a sandbank of finite horizontal extent. He investigated the impulse response to an isolated hump but neglected Coriolis effects and considered only bed load transport. More recently, the same type of model was applied in relation to human intervention at the seabed. *Roos et al.* [2001] used the results of a stability analysis to describe the evolution of large-scale offshore sandpits. *Fluit and Hulscher* [2002] and *Roos and Hulscher* [2002] used similar models to describe the seabed evolution induced by a gas-mined seabed depression. Recently, *Van de Kreeke et al.* [2002] studied the evolution of a trench cross section subject to an asymmetric tide (perpendicular to the trench axis), leading to predictions of trench migration and diffusion.

[5] We will show that the various elements in the linear modeling of offshore morphodynamics follow from the concept of impulse response, as depicted in Figure 1, to either the isolated ridge (a one-dimensional impulse, as the topography depends on only one horizontal coordinate) or the isolated hump (a two-dimensional impulse) (Figure 1). The former represents a novel approach, which is tailored to the analysis of arbitrary, one-dimensional topographies, such as sandbanks and dredged trenches. The latter, designed to study arbitrary (two-dimensional) topographies, is an extension of earlier results by *Huthnance* [1982b] by including Coriolis effects, considering both bed load and suspended load transport, and allowing for asymmetric flow. The bed response consists of growth or decay of the ridge or hump itself, possible migration effects due to tidal asymmetry along with sedimentation, and erosion patterns around the ridge or hump. The one-dimensional impulse will be used to study sandbank formation, reproducing the results of earlier analysis, as well as the evolution of a dredged trench, whereas the two-dimensional impulse will be used in a study of offshore sandpits or sandbanks of finite horizontal extent (Figure 1).

[6] Closer to the coast, sandy shelf seas like the North Sea usually exhibit large-scale features that differ from the offshore tidal sandbanks discussed above. For the formation and evolution of these so-called shoreface-connected ridges, alternative models have been developed in which the presence of a coastline and a sloping inner shelf are crucial elements [*Trowbridge*, 1995; *Calvete et al.*, 2002, and references therein].

[7] In section 2 we describe the morphodynamic model, with particular attention paid to the process of linearization; Figure 2 explains general concepts of morphodynamic modeling. In section 3 we derive the response to an isolated ridge, use it to obtain the results of a linear stability analysis, and discuss similarities. Section 4 focuses on the evolution of a dredged channel. We present the response to the isolated hump in section 5. The physical mechanisms are explained in Figure 9. Section 6 contains its application in the study of offshore sandpits (or sandbanks of finite horizontal extent). Finally, section 7 presents the discussion, conclusions, and an outlook on future research, with particular attention to comparing data and modeling as described in this paper (Figures 13 and 14).

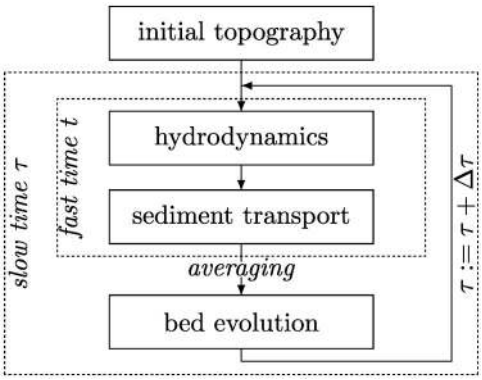

Figure 2. The essential elements in morphodynamic modeling. They are found in the morphological loop, which we explain here for the case of a tidally dominated offshore environment. The separation in two timescales is important, with a fast time t for the hydrodynamics and sediment transport within the tidal cycle (half a day) and a slow time τ for the seabed evolution (decades to centuries). After specifying an initial topography, the next step is to solve the hydrodynamics, i.e., to determine currents, tides, and waves. These processes are defined on the fast time, i.e., within the tidal cycle. For large-scale computations in a shallow water domain a depth-averaged approach is usually suitable, and the Coriolis force and bottom friction should be included. The tidally averaged flow pattern, called the residual flow, can be nonzero even if the hydrodynamic forcing itself is symmetric (Figure 9). Depending on flow conditions and sediment characteristics, noncohesive sediment can be transported in two modes: either rolling and sliding close to the seabed, i.e., as bed load, or picked up and carried in suspension by the flow, i.e., as suspended load. Semiempirical formulas exist to model the bed load flux and the entrainment of suspended matter, usually expressed in terms of the bed shear stress but expressed here as a function of the depth-averaged flow quantities. Divergences of the bed load flux along with the difference between entrainment and deposition of suspended matter cause erosion or sedimentation throughout the domain. However, these bed changes are so slow that only the tidal average of the sediment transport matters. We thus end up with an updated topography at a new level in morphodynamic time.

2. THE MODEL

2.1. Flow, Sediment Transport, and Bed Evolution

[8] We refer to Figure 2 for general concepts of morphodynamic modeling in a tidally dominated environment. Consider a tidal wave with maximum velocity U^* and tidal frequency σ^* in an offshore part of a shallow sea of undisturbed depth H^*. Unsteady flow can be described by the depth-averaged shallow water equations, i.e., by two momentum equations and a mass balance. In dimensional form (an asterisk denotes a dimensional quantity) the model reads

$$g^*\nabla^* z_s^* + \frac{\partial \mathbf{u}^*}{\partial t^*} + \mathbf{u}^*\cdot\nabla^*\mathbf{u}^* + f^*\mathbf{e}_z\times\mathbf{u}^* + \frac{r^*\mathbf{u}^*}{H^* + z_s^* - z_b^*} = 0 \quad (1)$$

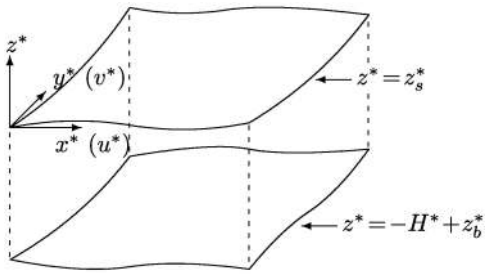

Figure 3. Definition sketch of the model geometry.

$$\frac{\partial z_s^*}{\partial t^*} - \frac{\partial z_b^*}{\partial t^*} + \nabla^*\cdot[(H^* + z_s^* - z_b^*)\mathbf{u}^*] = 0. \quad (2)$$

Here $\mathbf{u}^* = (u^*,v^*)$, which are the velocity components in the directions of the horizontal coordinates $\mathbf{x^*} = (x^*,y^*)$, respectively, and we define $\nabla^* = (\partial/\partial x^*,\partial/\partial y^*)$. The z^* axis, with unit vector $\mathbf{e}_z = (0,0,1)$, points upward with the free surface elevation at $z^* = z_s^*$ and the bed level at $z^* = -H^* + z_b^*$ (Figure 3). Furthermore, g^* is the gravitational acceleration, effects of the Earth's rotation are accounted for by Coriolis parameter f^*, t^* is time, and we adopt a linear friction law with parameter r^*. The boundaries of the offshore system are taken infinitely far away.

[9] The seabed is assumed to consist of cohesionless sediment of uniform size, which is transported as bed load or as suspended load. The volumetric bed load sediment flux (in $m^2\,s^{-1}$) is described by a generalization of an empirical relationship, which includes a slope correction [see, e.g., *Van Rijn*, 1993]:

$$\mathbf{S}^* = \alpha_b^*|\mathbf{u}^*|^{\beta_b}\left(\frac{\mathbf{u}^*}{|\mathbf{u}^*|} - \lambda^*\nabla^* z_b^*\right). \quad (3)$$

Three parameters appear: the proportionality parameter α_b^*; the power β_b, usually valued between 3 and 5, reflecting the faster than linear dependency of sediment transport on the flow velocity; and the bed slope parameter λ^*, quantifying the downhill preference of moving sediment. Values for these parameters, taken from *Hulscher et al.* [1993], are given in dimensionless form in section 2.2.

[10] Suspended load transport requires a different description. The depth-averaged volumetric concentration c^* can be described by an advection equation [*De Vriend*, 1990]:

$$\frac{\partial c^*}{\partial t^*} + \mathbf{u}^*\cdot\nabla^* c^* = \frac{\alpha_s^*|\mathbf{u}^*|^{\beta_s}}{H^* + z_s^* - z_b^*} - \gamma^* c^*. \quad (4)$$

The right-hand side models the exchange between bed and fluid column due to entrainment and deposition. Entrainment is assumed to be proportional to some power β_s of the depth-averaged flow velocity magnitude (usually 2 [*Dyer*, 1986]), with a factor α_s^*. The deposition is proportional to c^* with factor γ^*. We neglect the diffusion of suspended sediment.

[11] The local rate of bed change is due then to both the divergences in bed load transport and the difference between deposition and entrainment, i.e.,

$$(1-\epsilon_p)\frac{\partial z_b^*}{\partial t^*} + \nabla^*\cdot\mathbf{S}^* + \alpha_s^*|\mathbf{u}^*|^{\beta_s} - \gamma^*(H^* + z_s^* - z_b^*)c^* = 0. \quad (5)$$

Here ϵ_p is the bed porosity (usually ~0.4). We limit our study to offshore situations where wave effects on sediment transport, other than those incorporated in α_b^* and α_s^* such as stirring, can be neglected.

2.2. Scaling Procedure and Timescales

[12] Next, the model is cast in nondimensional form, in which we furthermore distinguish two timescales. By introducing the scaled variables

$$\mathbf{u} = \frac{\mathbf{u}^*}{U^*}, \quad t = \sigma^* t^*, \quad \mathbf{x} = \frac{\sigma^*\mathbf{x}^*}{U^*}, \quad z_b = \frac{z_b^*}{H^*},$$
$$z_s = \frac{g^* z_s^*}{U^{*2}}, \quad \mathbf{S} = \frac{\mathbf{S}^*}{\alpha_b^* U^{*\beta_b}}, \quad c = \frac{\gamma^* H^* c^*}{\alpha_s^* U^{*\beta_s}}, \quad (6)$$

we arrive at the following nondimensional model:

$$\nabla z_s + \frac{\partial \mathbf{u}}{\partial t} + \mathbf{u}\cdot\nabla\mathbf{u} + f\mathbf{e}_z\times\mathbf{u} + \frac{r\mathbf{u}}{1-z_b} = 0, \quad (7)$$

$$\nabla\cdot[(1-z_b)\mathbf{u}] = 0, \quad (8)$$

$$\mathbf{S} = |\mathbf{u}|^{\beta_b}\left(\frac{\mathbf{u}}{|\mathbf{u}|} - \lambda\nabla z_b\right), \quad (9)$$

$$A\left[\frac{\partial c}{\partial t} + \mathbf{u}\cdot\nabla c\right] = \frac{|\mathbf{u}|^{\beta_s}}{1-z_b} - c, \quad (10)$$

$$\frac{\partial z_b}{\partial \tau} + \hat{\alpha}_b\nabla\cdot\langle\mathbf{S}\rangle + \frac{\hat{\alpha}_s}{A}\langle|\mathbf{u}|^{\beta_s} - (1-z_b)c\rangle = 0. \quad (11)$$

Here $\nabla = (\partial/\partial x, \partial/\partial y)$. We have omitted terms proportional to $Fr^2 = U^{*2}/(g^*H^*)$, corresponding to a rigid lid approach. The angle brackets denote tidal averaging.

[13] The model contains two timescales. Besides the fast hydrodynamic timescale t, we have introduced a slow morphodynamic timescale τ, associated with the strongest of the two types of sediment transport:

$$\tau = \mu t, \qquad \mu = \max(\alpha_b, \alpha_s). \quad (12)$$

We assume that the flow and sediment transport quantities evolve on both timescales t and τ, whereas the seabed z_b evolves only on the slow timescale τ. Hence the fast bed changes within the tidal cycle ($\partial z_b/\partial t$) are neglected, which effectively decouples the hydrodynamics and sediment transport (equations (7)–(10)) from the bed evolution (equation (11)); this is a quasi-stationary approach. Moreover, in equation (11) only the tidally averaged sediment transport contributes to the bed evolution.

[14] In the scaled model and the slow timescale τ the following nondimensional parameters appear:

$$r = \frac{r^*}{\sigma^* H^*}, \quad f = \frac{f^*}{\sigma^*}, \quad \lambda = \frac{H^*\sigma^*\lambda^*}{U^*}, \quad A = \frac{\sigma^*}{\gamma^*},$$
$$\hat{\alpha}_b = \frac{\alpha_b}{\mu}, \quad \alpha_b = \frac{\alpha_b^* U^{*\beta_b - 1}}{(1-\epsilon_p)H^*}, \quad (13)$$
$$\hat{\alpha}_s = \frac{\alpha_s}{\mu}, \quad \alpha_s = \frac{\alpha_s^* U^{*\beta_s}}{(1-\epsilon_p)H^*\gamma^*}.$$

Here A is the ratio of the timescale of the deposition process for suspended sediment and the tidal period. Appropriate parameter values are $r = 0.237-2.37$, $f = 0.83$, $\lambda = 0.0084$, $A = 0.01$, $\alpha_b = 5\times10^{-7} - 5\times10^{-6}$, and $\alpha_s = 1.5\times10^{-4}$. Note that, by definition of τ in equation (12), either $\hat{\alpha}_b$ or $\hat{\alpha}_s$ equals one. The other is smaller and can be set to zero to isolate the transport mechanisms from each other.

[15] We will further simplify by omitting inertial terms, i.e., $\partial\mathbf{u}/\partial t$ from the momentum equation (7) and $\partial c/\partial t$ from the concentration equation (10). This means that the flow adapts instantaneously to changes in the tidal forcing, and the sediment concentration adapts instantaneously to changes in the flow. *Huthnance* [1982a] and *De Vriend* [1988] have shown that neglecting inertial terms hardly affects the stability properties of the flat seabed.

2.3. Basic State and Linearization

[16] The morphodynamic model consists of a set of nonlinear equations which cannot be solved in closed form. Hence we resort to an approximation technique. Let

$$\phi = (\mathbf{u}, z_b, \nabla z_s, \mathbf{S}, c) \quad (14)$$

denote the state of the system. The spatially uniform but time-dependent state ϕ_0, given by

$$\phi_0 = (\mathbf{u}_0, 0, (\nabla z_s)_0, \mathbf{S}_0, c_0), \quad (15)$$

is a solution to the set of equations. It describes a flat bed subject to a spatially uniform tidal flow and will be called the basic state. For the basic flow $\mathbf{u}_0$ one can take various representations, such as a unidirectional current [*Huthnance*, 1982a, 1982b], a sinusoidal M_2 component in one direction [*Huthnance*, 1982a], or one with a certain ellipticity [*Hulscher et al.*, 1993], possibly including a residual M_0 component and an M_4 overtide [*Roos et al.*, 2001]. We keep the basic flow as simple as possible, while still allowing it to mimic tidal (a)symmetry. To that end, we propose a block flow inclined at an angle θ with respect to the x axis:

$$\mathbf{u}_0(t) = I(t)(\cos\theta, -\sin\theta),$$
$$I(t) = \begin{cases} I_1 & 0 \le t/(2\pi) < \delta \\ I_2 & \delta \le t/(2\pi) < 1 \end{cases}, \quad (16)$$

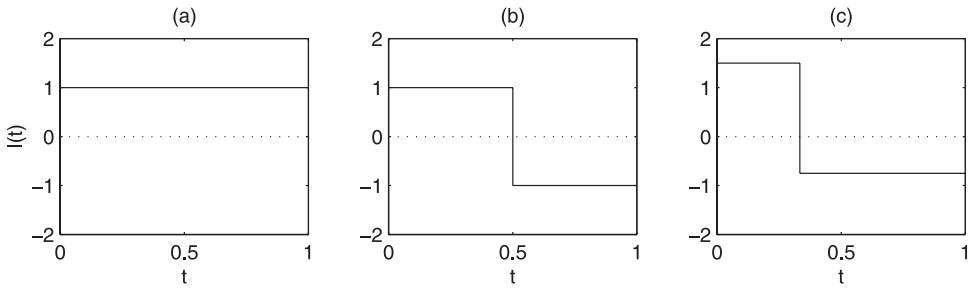

Figure 4. Examples of the basic flow (equation (16)), i.e., plots of $I(t)$ in three cases: (a) steady current ($I_1 = \delta = 1$), (b) symmetric block flow ($I_1 = -I_2 = 1$ and $\delta = 1/2$), and (c) asymmetric block flow ($I_1 = 3/2$, $I_2 = -3/4$, and $\delta = 1/3$).

with $I_1 > 0$, $I_2 < 0$, and $0 \leq \delta \leq 1$ (Figure 4). In particular, for $I_1 = -I_2 = 1$ and $\delta = 1/2$ we recover the symmetric block tide studied previously by *Huthnance* [1982a]. He showed that in a linear stability analysis a symmetric block tide and an M_2 tide give qualitatively similar results. As we neglect inertial terms, the flow and bed response averaged over a tidal cycle reduce to the weighted average of the responses to two steady currents I_1 and I_2 with weighting factors δ and $1 - \delta$, respectively. A uniform free surface slope $(\nabla z_s)_0$ acts as the pressure gradient that drives the basic flow. The basic flow induces sediment transport, i.e., nonzero $\mathbf{S}_0$ and c_0. However, it does not trigger any bed evolution as, in equation (11), $\nabla \cdot \mathbf{S}_0 = 0$, and c_0 equals the reference concentration $|\mathbf{u}_0|^{\beta s}$.

[17] We consider the topographies as perturbations of the flat bed, which are small compared to the water depth. Introducing the small nondimensional amplitude $\epsilon = \epsilon^*/H^*$, we can define the isolated ridge and the isolated hump (see Figure 1) by

$$z_b = \epsilon\delta(x), \qquad z_b = \epsilon\delta(x)\delta(y), \tag{17}$$

respectively. Here $\delta(\ )$ is the Dirac function: $\delta(\xi) = 0$ for $\xi \neq 0$ and $\int_J \delta(\xi)d\xi = 1$ if $0 \in J$. As $\epsilon \ll 1$, the state corresponding to the topographies (equation (17)) is likely to be a small perturbation of the basic state ϕ_0, i.e., of order ϵ. So let us expand linearly around the basic state according to

$$\phi = \phi_0 + \epsilon\phi_1 + \mathbb{O}(\epsilon^2). \tag{18}$$

We neglect higher-order terms with respect to the linear ones in ϵ, so solving the problem for ϕ reduces to solving a linear problem for ϕ_1. This linear problem follows from substituting equation (18) in the model equations and collecting terms of order ϵ:

$$\nabla z_{s1} + \mathbf{u}_0 \cdot \nabla \mathbf{u}_1 - f\mathbf{e}_z \times \mathbf{u}_1 + r(z_{b1}\mathbf{u}_0 + \mathbf{u}_1) = 0, \tag{19}$$

$$\nabla \cdot \mathbf{u}_1 - \mathbf{u}_0 \cdot \nabla z_{b1} = 0, \tag{20}$$

$$\mathbf{S}_1 = |\mathbf{u}_0|^{\beta_b - 1}\mathbf{u}_1 + (\beta_b - 1)|\mathbf{u}_0|^{\beta_b - 3}(\mathbf{u}_0 \cdot \mathbf{u}_1)\mathbf{u}_0 - \lambda|\mathbf{u}_0|^{\beta_b}\nabla z_{b1}, \tag{21}$$

$$A\mathbf{u}_0 \cdot \nabla c_1 = \beta_s|\mathbf{u}_0|^{\beta_s - 2}\mathbf{u}_0 \cdot \mathbf{u}_1 - c_1 + c_0 z_{b1}, \tag{22}$$

$$\frac{\partial z_{b1}}{\partial \tau} + \hat{\alpha}_b \nabla \cdot \langle \mathbf{S}_1 \rangle + \frac{\hat{\alpha}_s}{A}\langle \beta_s|\mathbf{u}_0|^{\beta_s - 2}\mathbf{u}_0 \cdot \mathbf{u}_1 - c_1 + c_0 z_{b1} \rangle = 0. \tag{23}$$

The model in this form serves as the starting point for the further analysis.

3. ONE-DIMENSIONAL IMPULSE RESPONSE: THE ISOLATED RIDGE

3.1. Definition and Green's Function

[18] In this section we investigate the evolution of an isolated ridge aligned with the y axis:

$$z_{b1} = \delta(x) \qquad [\tau = 0]. \tag{24}$$

As both basic flow (equation (16)) and initial profile (equation (24)) are independent of y, so will the topography be as it evolves in time. Let the bed evolution starting from equation (24) be given by $z_{b1} = G(x, \tau)$, called Green's function. Then, for an arbitrary yet y-independent initial topography, the bed evolution follows from the convolution integral of Green's function and topography, i.e.,

$$z_{b1}(x, \tau) = \int_{-\infty}^{\infty} G(\xi,\tau) z_{b1}^{\text{init}}(x - \xi)d\xi. \tag{25}$$

However, an analytical expression for G cannot be found in closed form. To facilitate the analysis, we therefore restrict to the initial response, and we define $\langle \chi(x) \rangle \equiv \partial G/\partial\tau$ at $\tau = 0$. In this case we find analytical expressions that give insight into the model's behavior.

3.2. Flow Response

[19] The flow over the ridge is decelerated by continuity and deflected by friction-topography and Coriolis-topography interactions (see also Figure 2). Indeed, from the continuity equation (20) and the momentum equation (19) in y direction we find

$$u_1 = I\delta(x)\cos\theta \tag{26}$$

$$v_1 = I(r\tan\theta - f)e^{-rx/(I\cos\theta)}H(Ix). \tag{27}$$

Here $H(\ )$ is the Heaviside function: Its value is unity for a positive argument and zero otherwise. The exponential decay of v_1 downstream of the ridge is due to advection and bottom friction, where the parameter $|I|r^{-1}\cos\theta$ determines the (e-folding) length of hydrodynamic influence. In the limiting case $\theta = \pm\pi/2$, i.e., when the basic flow is aligned with the ridge, this length vanishes, and the flow response reduces to $\mathbf{u}_1 = (0, I\delta(x))$. The momentum equation in x direction can be used to find z_{s1}, which we do not pursue here as it does not contribute to the bed evolution.

3.3. Bed Evolution for Bed Load Transport

[20] The perturbed bed load sediment flux $\mathbf{S}_1$ follows from substituting the basic flow equation (16) along with the perturbed velocities equations (26) and (27) into the linearized transport formula (21). Next, the bed evolution equation (23) with $\hat{\alpha}_s = 0$ (no suspended load) leads to an evolution equation for arbitrary topographies $z_{b1}(x)$:

$$\frac{\partial z_{b1}}{\partial\tau} = -\rho_{b1}\frac{\partial z_{b1}}{\partial x} + \rho_{b2}\frac{\partial^2 z_{b1}}{\partial x^2} + P(\theta)\left[\rho_{b0}z_{b1} - \int_{-\infty}^{\infty}\rho_{b3}(\xi)z_{b1}(x-\xi)d\xi\right]. \tag{28}$$

The nonnegative ρ_{b0}, ρ_{b1}, ρ_{b2}, and $\rho_{b3}(x)$ are specified in Appendix A; $P(\theta)$ will be specified and analyzed below. Because of the structure of $\rho_{b3}(x)$ we cannot solve equation (28) in a convenient closed form, except when $P(\theta) = 0$.

[21] Neglecting the term in $P(\theta)$ for the moment, the evolution equation (28) reduces to an advection-diffusion equation, leading to

$$G_{b0}(x,\tau) = \frac{1}{\sqrt{4\pi\rho_{b2}\tau}}\exp\left[\frac{-(x-\rho_{b1}\tau)^2}{4\rho_{b2}\tau}\right]. \tag{29}$$

The migration term ρ_{b1} is nonzero only in the case of asymmetric block flow not parallel to the ridge ($\theta \neq \pm\pi/2$). The diffusion of the ridge is directly associated with bed slope effects.

[22] The last term of equation (28) disrupts its advective-diffusive character by introducing an additional redistribution of sediment. The sign and magnitude of $P(\theta)$, given by

$$P(\theta) = \sin\theta(r\sin\theta - f\cos\theta), \tag{30}$$

determines its character and importance, respectively. The quantity $P(\theta)$ combines frictional and Coriolis effects with the basic flow angle. We identify two parts. Evolution of the form itself is incorporated in the term in ρ_{b0}, and the sign of $P(\theta)$ determines whether this is growth or decay. The form decays for $0 < \tan\theta < f/r$ (assuming $f > 0$, which applies to the Northern Hemisphere); it is unaffected for $\theta = 0$ or $\theta = \arctan f/r$ and grows otherwise. Apparently, Coriolis effects disturb the symmetry about $\theta = 0$. Form decay is strongest for $\theta_d = \frac{1}{2}\arctan f/r$, while form growth is maximal for $\theta_g = \frac{1}{2}(\arctan f/r - \pi)$. These properties of $P(\theta)$ (depicted in Figure 6a) again show up in a harmonic stability analysis (see section 3.5). The amount of sand involved in form growth (or decay) equals the surrounding erosion (or sedimentation), given by $\rho_{b3}(x)$. Possible asymmetry of the basic flow will cause $\rho_{b3}(x)$ to be asymmetric in x.

3.4. Bed Evolution for Suspended Load Transport

[23] The perturbed concentration follows from substituting the basic flow equation (16) and the flow response equations (26) and (27) into the equations for suspended load transport equation (22) (Appendix A). Substituting the result and the perturbed velocities into equation (23) with $\hat{\alpha}_b = 0$ (no bed load transport) and taking the tidal average now results in an evolution equation for arbitrary topographies $z_{b1}(x)$:

$$\frac{\partial z_{b1}}{\partial\tau} = -\rho_{s0}z_{b1} + \int_{-\infty}^{\infty}[P(\theta)\rho_{s31}(\xi) + \rho_{s32}(\xi)]z_{b1}(x-\xi)d\xi. \tag{31}$$

The nonnegative ρ_{s0} along with $\rho_{s31}(x)$ and $\rho_{s32}(x)$ are specified in Appendix A. The form now always turns out to be decaying as $\rho_{s0} > 0$. In contrast with the bed load case we find neither migration nor diffusion terms. Migratory effects are contained in the scour or deposition function $\rho_{s3}(x)$, which is more complicated than in the bed load case. It involves terms exponentially decaying determined by friction and advection of sediment, respectively. The amount of sand released by the form decay equals surrounding deposition, given by the convolution term in ρ_{s32}.

[24] Finally, we can link the two transport mechanisms by noting that, for $\beta_s = \beta_b - 1$, $\lambda = 0$, and in the limit $A \downarrow 0$, the bed evolution equations (28) and (31) become identical. This means that, neglecting bed slope effects, bed load transport is a special case of suspended load transport in the limit of zero advection.

3.5. Relation With Harmonic Stability Analysis: Sandbank Formation

[25] Here we will apply the general bed evolution equations (28) and (31) to a wavy topography $z_{b1} = a(\tau)\cos kx$. These are the eigenfunctions of the linearized system, so we actually perform a harmonic stability analysis [*Huthnance*, 1982; *De Vriend*, 1990; *Hulscher et al.*, 1993]. Such an analysis, aimed at explaining the formation of tidal sandbank patterns in, for example, the

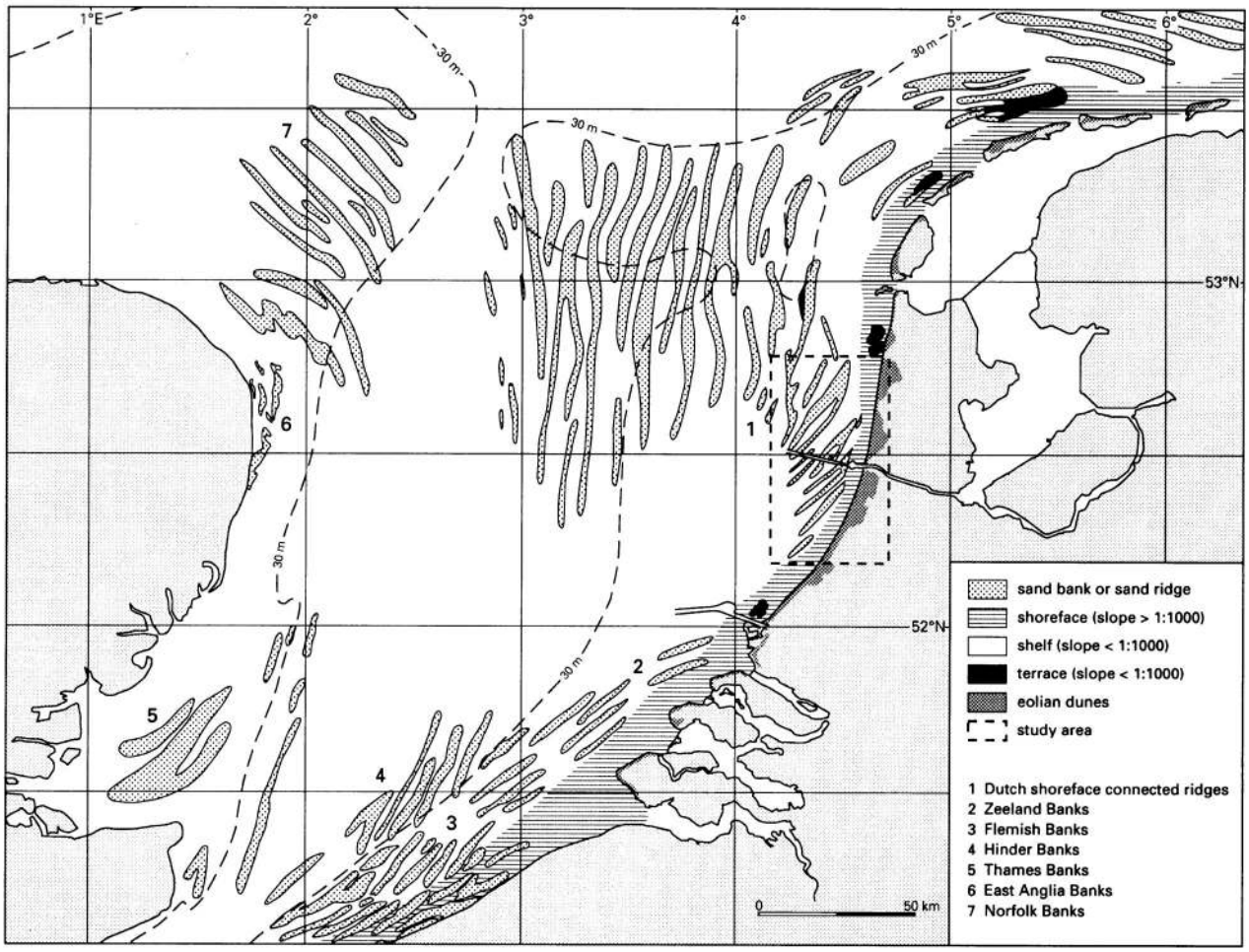

Figure 5. Sandbank patterns in the southern part of the North Sea [*Van de Meene*, 1994].

North Sea (Figure 5) predicts exponential growth or decay along with migration:

$$z_{b1}(x, \tau) = e^{\omega_r \tau}\cos(kx - \omega_i t), \qquad \omega = \omega_r + i\omega_i. \tag{32}$$

The growth rate ω is a complex number that depends both on the orientation θ of the perturbation with respect to the tide and on its wavelength $2\pi/k$, as well as on the Coriolis parameter f, friction coefficient r, sediment transport parameters β_b, λ, A, and β_s, and on the characteristics of the basic flow $\mathbf{u}_0$. The real part determines the growth or decay, whereas the imaginary part is associated with migration.

[26] For a symmetric block flow (Figure 4b) the growth rate is real and, in the case of bed load transport, given by

$$\omega_b = \frac{(\beta_b - 1)P(\theta)k^2\cos^2\theta}{r^2 + k^2\cos^2\theta} - \lambda k^2. \tag{33}$$

This agrees with the results found by *Huthnance* [1982a] and *Fluit and Hulscher* [2002]. As equation (33) is based on a symmetric block flow, we cannot compare this result with growth rates that correspond to alternative, more realistic types of basic flow [*Huthnance*, 1982a; *De Vriend*, 1990; *Hulscher et al.*, 1993] (section 2.3). The mode for which the real part of the growth rate is greatest is called the fastest growing mode (FGM), depicted in Figure 6b. Its characteristics $k_{\mathrm{fgm}} \approx 4$ and $\theta_{\mathrm{fgm}} \approx -60°$ correspond to dimensional wavelengths between 5 and 10 km and crests oriented counterclockwise at 30° with respect to the tidal current. This agrees with the characteristics of tidal sandbanks in the North Sea.

[27] For suspended load transport the expression for the growth rate is more complicated:

$$\omega_s = \frac{\beta_s P(\theta)k^2\cos^2\theta}{r^2 + k^2\cos^2\theta}\left[\frac{1 + Ar}{1 + A^2k^2\cos^2\theta}\right] - \frac{Ak^2\cos^2\theta(1 + \beta_s\cos^2\theta)}{1 + A^2k^2\cos^2\theta}. \tag{34}$$

We identify the following three properties of suspended load transport (Figure 6). First, it promotes the growth of features with crests slightly more aligned with the flow than in the case of bed load transport [*De Vriend*, 1990]. Second, the absence of a diffusive bed slope mechanism causes the lobes with positive growth rates to be unbounded, which is physically unrealistic. However, like

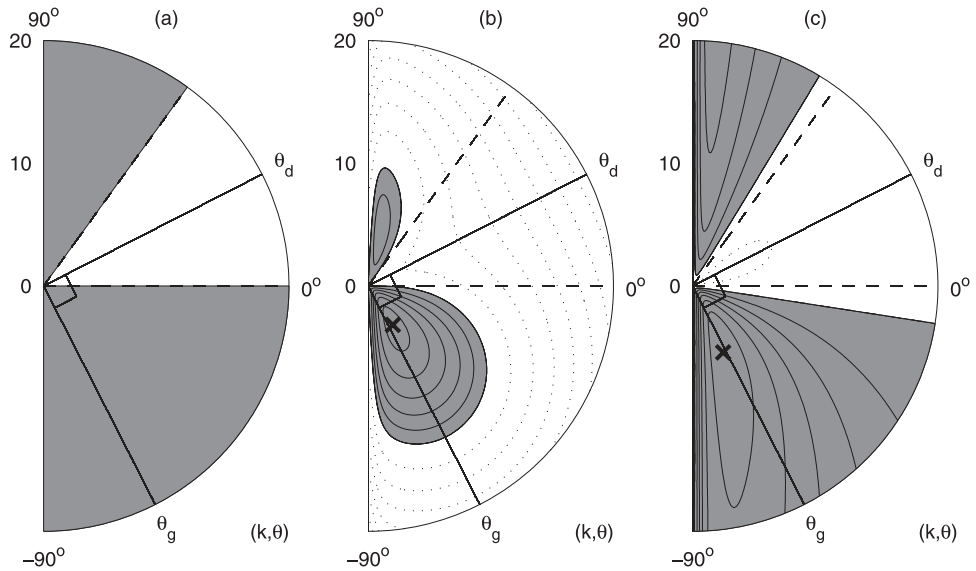

Figure 6. Stability properties of the flat seabed in polar (k,θ) plots. (a) Properties of $P(\theta)$, i.e., the region $P(\theta) > 0$ (shaded) and $P(\theta) < 0$ (open), along with the angles of maximum decay θ_d and maximum growth θ_g (solid lines). Contour plots of typical growth rates for (b) bed load and (c) suspended load. Shading and solid contours indicate positive growth rates; open areas and dotted contours indicate negative growth rates. Parameter values are the following: $r = 1$, $f = 0.83$, $\beta_b = 3$, $\lambda = 0.0084$, $\beta_s = 2$, and $A = 0.1$. The fastest growing mode is denoted with a cross.

bed load transport, suspended load is susceptible to bed slope effects [*Parker*, 1978; *Talmon et al.*, 1995]. Indeed, analogously to the bed load case, adding a bed slope term to the bed evolution equation (5) would solve this deficiency. Third, for $\beta_s = \beta_b - 1$ and $\lambda = 0$, we find that

$$\lim_{A \downarrow 0} \omega_s = \omega_b, \tag{35}$$

again showing that bed load transport acts as a limiting case of suspended load transport.

[28] Now let us revisit the role of the parameter $P(\theta)$ as given by equation (30). Besides controlling the dynamics of the ridge, it also tells us how the growth rates (equations (33) and (34)) of wavy features depend on their orientation θ. Indeed, in the θ interval $0 < \tan\theta < f/r$, where $P(\theta) < 0$, both the ridge and wavy perturbations decay. Moreover, positive growth rates only occur for θ values for which the ridge grows as well, i.e., when $P(\theta) > 0$. The parameter $P(\theta)$ obviously does not incorporate the damping of short wavelengths by the slope effect on bed load transport, which causes negative growth rates for large k. Finally, the angle $\theta_g = \frac{1}{2}(\arctan f/r - \pi)$ of maximal ridge growth turns out to predict the angle of the FGM well (Figures 6b and 6c).

[29] Green's function, introduced in section 3.1, can be expressed in terms of the obtained growth rates equations (33) and (34) according to

$$G(x, \tau) = \int_{-\infty}^{\infty} e^{\omega(k)\tau} e^{ikx} dk + \text{c.c.} \tag{36}$$

Here c.c. means complex conjugation. However, this integral is too complicated for further evaluation. Section 5 will show that the same holds for Green's function in two dimensions.

4. APPLICATION: EVOLUTION OF A DREDGED CHANNEL

[30] We now apply the bed evolution equation (28) for bed load transport to investigate the morphodynamic evolution of a dredged trench. Let us consider a Gaussian cross section, i.e.,

$$z_{b1}(x) = \frac{-1}{\sigma_{tr}\sqrt{\pi}} \exp\left[\frac{-(x - x_c)^2}{\sigma_{tr}^2}\right]. \tag{37}$$

The center of the trench is located at $x = x_c$, while σ_{tr} is a characteristic half width: At $x = x_c \pm \sigma_{tr}$, the trench depth is reduced by a factor $e^{-1} \approx 0.37$ (Figure 7a).

[31] For a basic flow that mimics an asymmetric tide (Figure 4c), we identify two qualitatively different kinds of behavior. First, for $P(\theta) > 0$, the trench migrates, and on both sides of the trench, additional humps appear, thus forming some sort of pattern of adjacent banks. This type of behavior closely follows the inherent instability of the flat seabed discussed in section 3.5 and depicted in Figure 6. Second, for $P(\theta) \leq 0$, the trench migrates, and diffusion causes the shape to flatten out toward a flat bed. As a special case we consider a basic flow perpendicular to the trench, i.e., $\theta = 0$ and $P(\theta) = 0$. The approximation (29) of Green's function is now

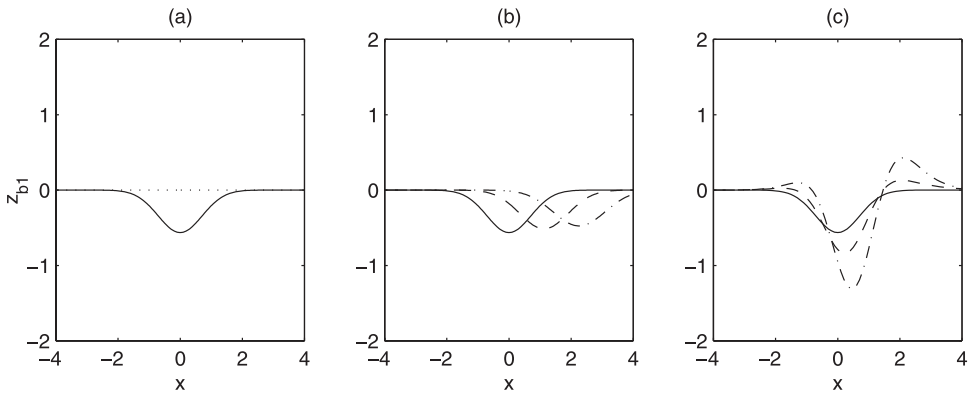

Figure 7. (a) Gaussian trench shape (equation (37)) with $\sigma = 1$ and $x_c = 0$. Evolution of this trench with bed load transport, subject to the forcing of Figure 4c, directed (b) perpendicular to the ridge ($\theta = 0$) and (c) at an angle $\theta = \theta_g \approx -63°$. Plotted is $z_{b1}(\tau)$ at $\tau = 0$ (solid), $\tau = 1/2$ (dashed), and $\tau = 1$ (dash-dotted). Parameter values are the following: $\beta = 3$ and $\lambda = 0.0084$.

exact. It predicts trench migration and diffusion, with trench center and width developing according to

$$x_c(\tau) = \rho_{b1}\tau, \qquad \sigma_{\mathrm{tr}}(\tau) = \sqrt{4\rho_{b2}\tau + \sigma_{\mathrm{tr},0}^2}, \tag{38}$$

with $\sigma_{\mathrm{tr},0}$ the half width at $\tau = 0$. The Gaussian shape equation (37) is thus preserved (Figure 7).

[32] With a model similar to the one presented here, *Van de Kreeke et al.* [2002] studied the morphodynamics of the access channel to the Port of Amsterdam. They report observations over a period of 2.3 years showing migration in the direction of net sediment transport at a rate of 2–4 m yr^{-1}. At the same time the channel widens and becomes shallower. In the model, *Van de Kreeke et al.* [2002] assumed tidal flow with M_0, M_2, and M_4 components, directed perpendicular to the trench, i.e., $\theta = 0$, and used parameter values much like the ones presented in section 2. This leads to migration estimates between 2.3 m yr^{-1} for bed load transport and 4.5 m yr^{-1} for suspended load transport, along with initial rates of half width increase of 0.4 m yr^{-1} and 2.5 m yr^{-1}, respectively. *Van de Kreeke et al.* [2002] furthermore showed that higher-order effects create asymmetry.

5. TWO-DIMENSIONAL IMPULSE RESPONSE: THE ISOLATED HUMP

5.1. Definition and Green's Function

[33] In this section we investigate the evolution of an isolated hump in the horizontal plane, given by

$$z_{b1} = \delta(x)\delta(y) \qquad [\tau = 0]. \tag{39}$$

The basic flow is given by equation (16), but contrary to the ridge case the orientation θ has become meaningless. Hence we choose $\theta = 0$, i.e., $\mathbf{u}_0 = (I, 0)$. The evolution starting from equation (39) now depends on both horizontal coordinates: $z_{b1} = G(x, y, \tau)$. The evolution of an arbitrary initial topography follows from the convolution integral of topography and Green's function, i.e.,

$$z_{b1}(x, y, \tau) = \int_{-\infty}^{\infty}\int_{-\infty}^{\infty} G(\xi, \zeta, \tau) z_{b1}^{\mathrm{init}}(x - \xi, y - \zeta) d\xi d\zeta. \tag{40}$$

As in the one-dimensional case, $G(x, y, \tau)$ cannot be found in a convenient closed form (in Appendix B we express G in terms of the growth rates obtained in section 3.5). We therefore restrict to the initial bed evolution: $\langle \chi(x,y) \rangle \equiv \partial G/\partial\tau$ at $\tau = 0$. For simplicity, we furthermore restrict to steady basic flow and symmetric basic flow (Figures 4a and 4b).

5.2. Flow Response

[34] It turns out that the problem can be conveniently solved in terms of the vorticity and the stream function. We therefore rewrite the flow equations (19) and (20) as

$$I\frac{\partial \eta_1}{\partial x} + r\eta_1 = I\left(r\frac{\partial z_{b1}}{\partial y} - f\frac{\partial z_{b1}}{\partial x}\right) \tag{41}$$

$$\nabla^2\psi_1 + \eta_1 = -I\frac{\partial z_{b1}}{\partial x}. \tag{42}$$

Here the vorticity is given by $\eta_1 \equiv \partial v_1/\partial x - \partial u_1/\partial y$, and the perturbed stream function ψ_1 satisfies $\partial\psi_1/\partial y = u_1 - z_{b1}u_0$ and $\partial\psi_1/\partial x = -v_1 + z_{b1}v_0$ (both are order ϵ quantities).

[35] We can divide equation (41) into two different problems, each of which can be solved with the aid of Green's representation theorem (Appendix B). To that end, we write

$$\eta_1 = \eta_r + \eta_f, \qquad \psi_1 = \psi_r + \psi_f, \tag{43}$$

effectively distinguishing a frictionally induced contribution and one due to Coriolis effects. In the tidally averaged sense the expressions read (Appendix B)

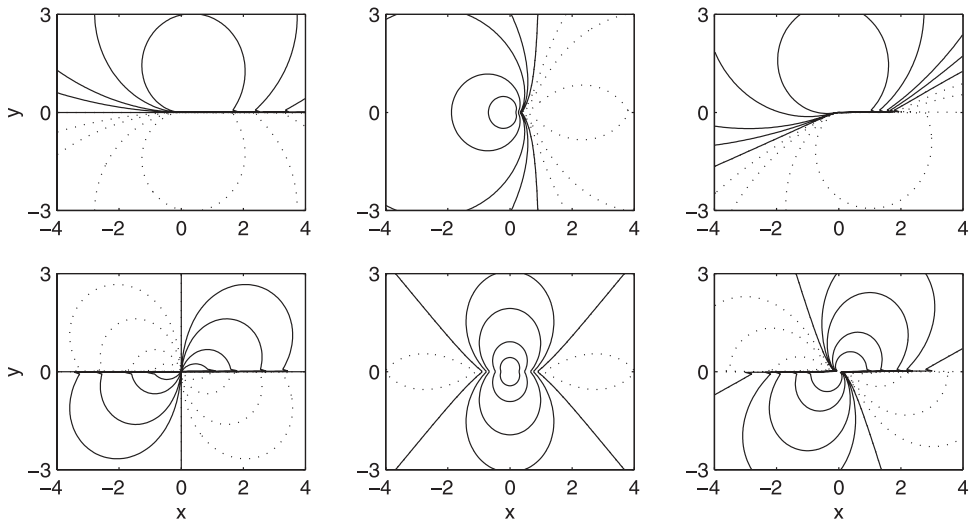

Figure 8. Perturbed stream function around a delta hump located at the origin, subject to (top) a steady current in the positive x direction and (bottom) a symmetric block flow along the x axis. Plotted are (left) ψ_r [*Huthnance*, 1982b], (center) Coriolis contribution ψ_f, and (right) the total stream function $\psi_1 \equiv \psi_r + \psi_f$. Solid contours indicate clockwise circulations; dotted contours indicate counterclockwise circulations. Parameter values are the following: $r = 1$ and $f = 0.83$.

$$\langle\psi_r\rangle = \frac{-ry}{4\pi}\int_0^\infty e^{-r\xi}\left\{\frac{1}{(x-\xi)^2+y^2} - \frac{1}{(x+\xi)^2+y^2}\right\}d\xi \tag{44}$$

$$\langle\psi_f\rangle = \frac{f}{4\pi}\left[\log(x^2+y^2) - \frac{r}{2}\int_0^\infty e^{-r\xi}\{\log[(x-\xi)^2+y^2] + \log[(x+\xi)^2+y^2]\}d\xi\right]. \tag{45}$$

The derivation of the frictionally induced contribution to the perturbed stream function is also given by *Huthnance* [1982b]. From equation (44), $\langle\psi_r\rangle$ is antisymmetric with respect to the x and y axis, while the Coriolis-induced contribution $\langle\psi_f\rangle$ is fully symmetric in both x and y. As a result, the only symmetry property of the sum $\langle\psi_1\rangle$ will be a point symmetry with respect to the origin. Hence plotting one quadrant of the (x, y) plane no longer suffices. Figure 8 shows how Coriolis effects alter the perturbed stream function obtained by *Huthnance* [1982b]. The cyclonically oriented circulation cells are amplified, whereas the anticyclonic ones are damped. Physically speaking, the increased friction above the isolated hump diverts the flow, while Coriolis effects disturb the symmetry of this pattern (see Figure 9).

5.3. Bed Evolution for Bed Load Transport

[36] The bed evolution equation (23) with $\hat{\alpha}_s = 0$ (no suspended load), combined with the linearized bed load transport formula (21), can be formulated in terms of the stream function ψ_1 according to

$$\frac{\partial z_{b1}}{\partial\tau} = -\beta_b\langle|I|^{\beta_b-1}I\rangle\frac{\partial z_{b1}}{\partial x} + \lambda\langle|I|^{\beta_b}\rangle\nabla^2 z_{b1} - (\beta_b - 1) \cdot \int_{-\infty}^{\infty}\int_{-\infty}^{\infty}\left\langle\left|I\right|^{\beta_b-1}\frac{\partial^2\psi_1}{\partial x\partial y}(\xi,\zeta)\right\rangle z_b(x-\xi, y-\zeta)d\xi\, d\zeta. \tag{46}$$

The first term on the right-hand side of equation (46) vanishes for a symmetric block flow. As in the one-dimensional case (section 3) the term in λ pertains to the downslope transport, which only acquires a meaning after we integrate over a sufficiently smooth topography by using equation (40). Analogous to equation (43), we write $\chi_b = \chi_{br} + \chi_{bf}$. *Huthnance* [1982b], who neglected Coriolis effects, identified three contributions to χ_{br}: (1) amplification of the form (the equivalent of ρ_{b0} and ρ_{s0} in section 3), (2) exponentially decaying scour downstream of the hump (the equivalent of $\rho_{b3}(x)$ and $\rho_{s3}(x)$ in section 3), and (3) a sedimentation and erosion function, which is defined in the horizontal plane and can be written as

$$\langle\chi_{br}\rangle = \frac{-(\beta_b-1)r}{2\pi}\int_0^\infty e^{-r\xi}\left\{\frac{(x-\xi)[(x-\xi)^2-3y^2]}{[(x-\xi)^2+y^2]^3} - \frac{(x+\xi)[(x+\xi)^2-3y^2]}{[(x+\xi)^2+y^2]^3}\right\}d\xi. \tag{47}$$

Each of these frictionally induced contributions is symmetric with respect to the x and y axis. The contribution χ_f due to Coriolis effects takes the following form:

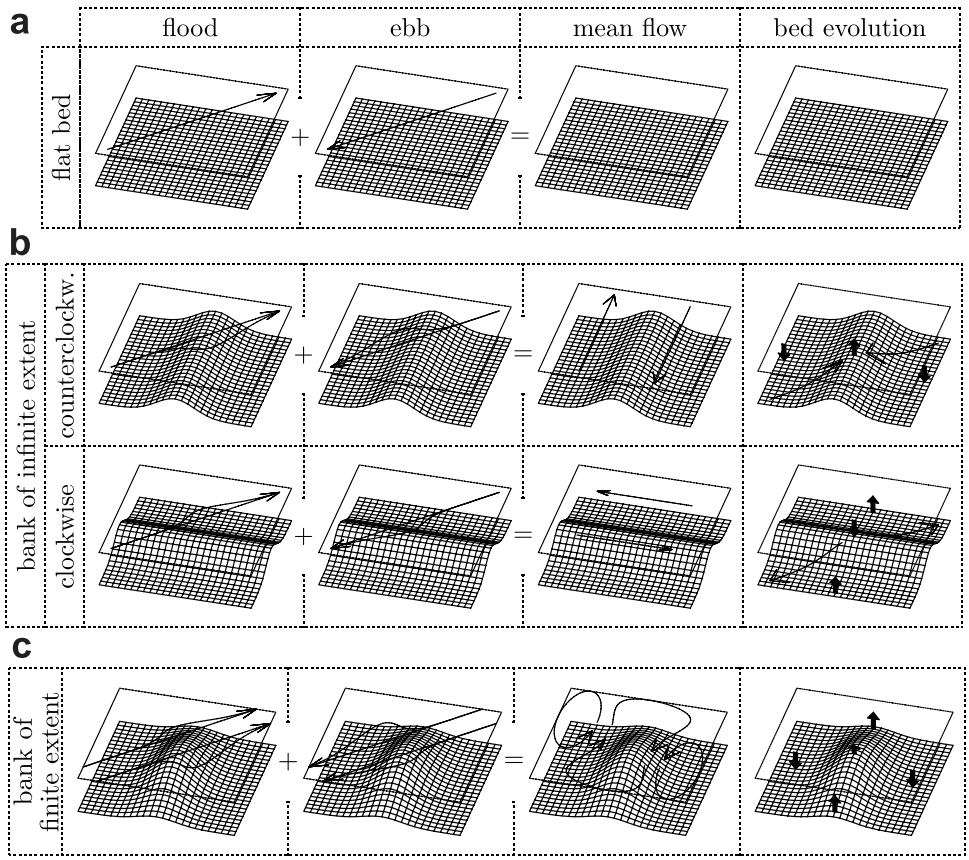

Figure 9. Physical mechanisms that induce the residual flow and the bed evolution in the case of a symmetrical tide. For each type of topography the three leftmost plots show the typical streamlines of the flow for the flood and ebb phase of the tidal cycle as well as the mean, i.e., tidally averaged flow pattern [see also *Zimmerman*, 1981; *Robinson*, 1983; *Pattiaratchi and Collins*, 1987; *Dyer and Huntley*, 1999]. In the case of a nonzero tidally averaged (bed load) sediment flux it is indicated by horizontal arrows in the rightmost plot, while the smaller vertical arrows indicate the corresponding bed evolution. (a) For a flat bed the flow is spatially uniform, and the tidal average vanishes. The tidally averaged sediment transport also vanishes, such that the seabed remains fully flat. This state is called the basic state. (b) In the case of a bank of infinite extent, i.e., a topography varying in one direction only, the flow is deflected by three mechanisms: (1) Continuity forces the cross-bank component of the flow to accelerate, (2) increased friction by reduced depth slows down the along-bank flow component, and (3) Coriolis-topography effects enhance cyclonic flow deflections (i.e., to the right on the Northern Hemisphere). The along-bank flow response is transported downstream by advection. In contrast with the flat bed case the tidal average is now nonzero and directed parallel to the bank contours. This residual flow can be seen as consisting of circulations around the bank, which are nonclosed because of the assumed infinite bank length. Depending on the orientation of the bank with respect to the flow, the friction-induced contribution to these circulations is clockwise (counterclockwise bank orientation, see the plot) or counterclockwise (clockwise bank orientation). On the Northern Hemisphere, Coriolis effects enhance the clockwise circulation, thus causing the flow response to be strongest for a bank with a counterclockwise orientation (see top row). Depending on the orientation of the bank, the tidally averaged sediment transport causes the bank either to (top) grow or (bottom) decay. (c) The same mechanisms apply to the more realistic case of a bank of finite extent, but the two-dimensionality of the topography complicates the picture. Increased friction diverts the flow around the bank, again with Coriolis effects enhancing clockwise deflections (on the Northern Hemisphere) and advection transporting the flow response downstream. The tidally averaged pattern exhibits three circulation zones: one above the bank with clockwise circulations, flanked by two zones with counterclockwise circulations. Clearly, the circulation cells are now closed because of the finite bank length, while Coriolis effects determine the sense of rotation of the main cell (clockwise on the Northern Hemisphere, counterclockwise on the Southern Hemisphere). The position, size, and shape of the cells depend on the exact topography, flow angle, and relative strength of Coriolis and frictional forces. The tidally averaged sediment transport pattern, more complex than in the previous cases and therefore not displayed here, tends to elongate the bank in the direction, which coincides with the preferred angle for one-dimensional banks.

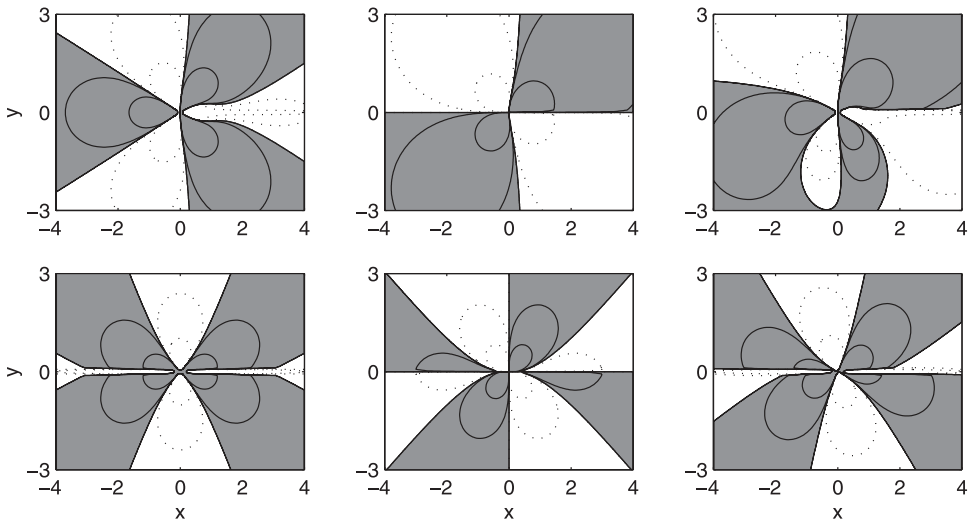

Figure 10. Initial sedimentation and erosion patterns around a delta hump located at the origin, subject to (top) a steady current in the positive x direction (χ) and (bottom) a symmetric block flow along the x axis ($\langle\chi\rangle$). Plotted are (left) χ_{br} [*Huthnance*, 1982b], (center) χ_{bf}, and (right) the total scour function $\chi_b \equiv \chi_{br} + \chi_{bf}$. Shaded and solid contours indicate deposition zones; open areas and dotted contours indicate erosion zones. Parameter values are the following: $r = 1$ and $f = 0.83$.

$$\langle\chi_{bf}\rangle = \frac{(\beta_b - 1)\,fxy}{\pi}\left\{\frac{1}{(x^2+y^2)^2} - \frac{r}{2}\int_0^\infty e^{-r\xi}\frac{y^4 + (x^2-\xi^2)(x^2+2y^2+3\xi^2)}{[(x-\xi)^2+y^2]^2[(x+\xi)^2+y^2]^2}\,d\xi\right\}. \quad (48)$$

It is easily seen that χ_{bf} is antisymmetric with respect to the x and y axis. The counterparts of equations (47) and (48) for steady flow can be found in Appendix B.

[37] The Coriolis-induced preference of the system for the formation and growth of cyclonically oriented features is clear from the ISE patterns (Figures 8 and 10). The underlying mechanisms have been discussed extensively in the context of wavy sandbank patterns [*Zimmerman*, 1981; *Robinson*, 1983; *Pattiaratchi and Collins*, 1987; *Dyer and Huntley*, 1999] (see also Figure 9), and we will do the same here for isolated features. Friction-topography and Coriolis-topography interactions generate vorticity (source terms in the vorticity equation (41)), which is advected downstream. The friction-topography interactions pertain to transverse bed slopes, giving rise to cells on both side sides of the hump (i.e., above and below the x axis). Consequently, the corresponding bed response χ_r is symmetric with respect to the x axis. In addition, Coriolis-topography interaction, dealing with streamwise bed slopes, causes cells upstream and downstream of the hump. The resulting Coriolis-induced bed response χ_f is antisymmetric with respect to the x axis, promoting deposition in the cyclonically oriented quadrants and erosion in the anticyclonically oriented ones. The net result is a relatively strong deposition in cyclonic direction, i.e., a preference for the formation and growth of cyclonically oriented features.

[38] The qualitative picture of the ISE patterns for steady flow (Figure 10, top left) resembles earlier results obtained with the method of characteristics. The analysis by *De Vriend* [1987a, 1987b] and the numerical experiments cited therein have shown that, in the absence of Coriolis effects, a hump subject to a steady flow develops into a pattern resembling a three-pointed star (Figure 11). Including the Coriolis force deforms the star shape, amplifying its cyclonic tip and weakening its anticyclonic tip.

5.4. Bed Evolution for Suspended Load Transport

[39] Now, we will discuss the method and results for the suspended load case. Combining the equations for suspended load transport (equations (22) and (23)) with $\hat{\alpha}_b = 0$ (no bed load transport) leads to the following set of equations, formulated in terms of the stream function:

$$c_1 + AI\frac{\partial c_1}{\partial x} = b\left(I\frac{\partial \psi_1}{\partial y} + z_{b1}\right) - AI\frac{\partial z_{b1}}{\partial x} \quad (49)$$

$$\frac{\partial z_{b1}}{\partial \tau} = -\left\langle I\frac{\partial c_1}{\partial x} + |I|^{\beta_s} + |I|^{\beta_s} I\frac{\partial z_{b1}}{\partial x}\right\rangle. \quad (50)$$

An expression for the concentration c_1 can be found in Appendix B. The bed evolution follows from equation (50) and contains elements similar to bed load transport. Analogously to the one-dimensional case, the advection parameter A of suspended load transport causes some smoothing in the x direction. However, the qualitative picture of the bed evolution is similar to the bed load case (already shown in Figure 10).

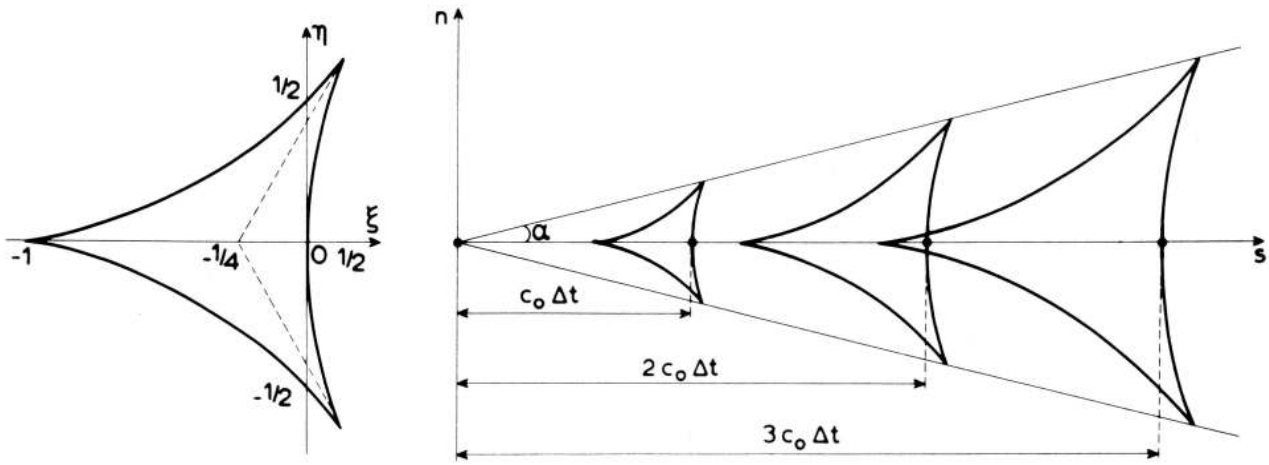

Figure 11. Evolution of a single hump subject to a steady flow from left to right according to characteristics analysis. Reprinted from *De Vriend* [1987a], copyright 1987, with permission from Elsevier Science.

6. APPLICATION: OFFSHORE SANDPIT

[40] In this section we study the evolution of an offshore sandpit from the perspective of the two-dimensional impulse response. For any topography of small bed amplitude $z_{b1}(x, y)$ the convolution integral (40) can be used to obtain the corresponding ISE. Because of the model's linearity in the bed amplitude the qualitative behavior for a pit on the one hand and a sandbank of finite horizontal extent (and of similar shape) on the other hand are identical, except for a sign change in flow and bed response. This means that clockwise residual circulations become counterclockwise, sedimentation zones become erosion zones, and vice versa.

[41] In the bed load case without Coriolis effects and for a symmetric block flow, *Huthnance* [1982b] used the two-dimensional impulse response χ_{br} to study the formation and growth of an individual sandbank. He investigated the subsequent bank evolution numerically, and the inclusion of nonlinear effects and some additional elements (wind waves and limited sand) led to equilibrium profiles.

[42] *Roos et al.* [2001] considered an offshore sandpit with a Gaussian shape in an otherwise flat bed and expressed it as a superposition of wavy features, i.e., the Fourier spectrum of the pit. In Fourier space, according to the individual growth rates of a linear stability analysis (bed load case, including Coriolis effects, and for an arbitrary tide consisting of an M_0, M_2, and M_4), the individual wavy features grow (or decay) exponentially with time. In physical space the pit evolution exhibits the following properties (see Figure 12): pit deepening, pit deformation, and possibly pit migration (in the case of tidal asymmetry) along with the formation of a bank pattern, which gradually grows, spreads, and possibly migrates around the pit. The spreading rate (elongation rate of the central pit or trough) is estimated at 12–120 m yr^{-1}; the migration rate is estimated at $\sim$ 1–7 m yr^{-1}. These estimates are based on conditions that apply to the southern part of the North Sea, comparable to those used by *Van de Kreeke et al.* [2002] (see also sections 2.2 and 4).

[43] The circulation cells and ISE patterns of the two-dimensional impulse response (section 5) resemble those of the bank or pit case [*Huthnance*, 1982b; *Roos et al.*, 2001], except for a sign change when comparing humps and pits. The convolution integral over the smooth topography of a pit or bank merely smears out the impulse response without disrupting the qualitative pattern.

7. DISCUSSION AND CONCLUSIONS

7.1. Interpretation and Relevance of the Topographic Impulse Response

[44] The generic value of the impulse response stems from the general bed evolution equations (28), (31), and (46). They govern the system's response to arbitrary topographies of small bed amplitude for both bed load and suspended load transport. The solution to these equations with an isolated ridge or hump as initial condition, called Green's function, mathematically contains all the information of the system's behavior. The response to an arbitrary topography at $\tau = 0$ follows from the convolution integrals (25) and (40). However, Green's function can generally not be derived in a convenient closed form. Only the special case $P(\theta) = 0$ leaves us with a simple advection-diffusion equation that can be solved exactly. Otherwise, we have to resort to numerical techniques or alternative approximations. Therefore we have mainly focused on the initial bed response.

[45] Finding a direct physical interpretation of the topographic impulses (equations (24) and (39)) is awkward. The concept of a finite mass being concentrated in

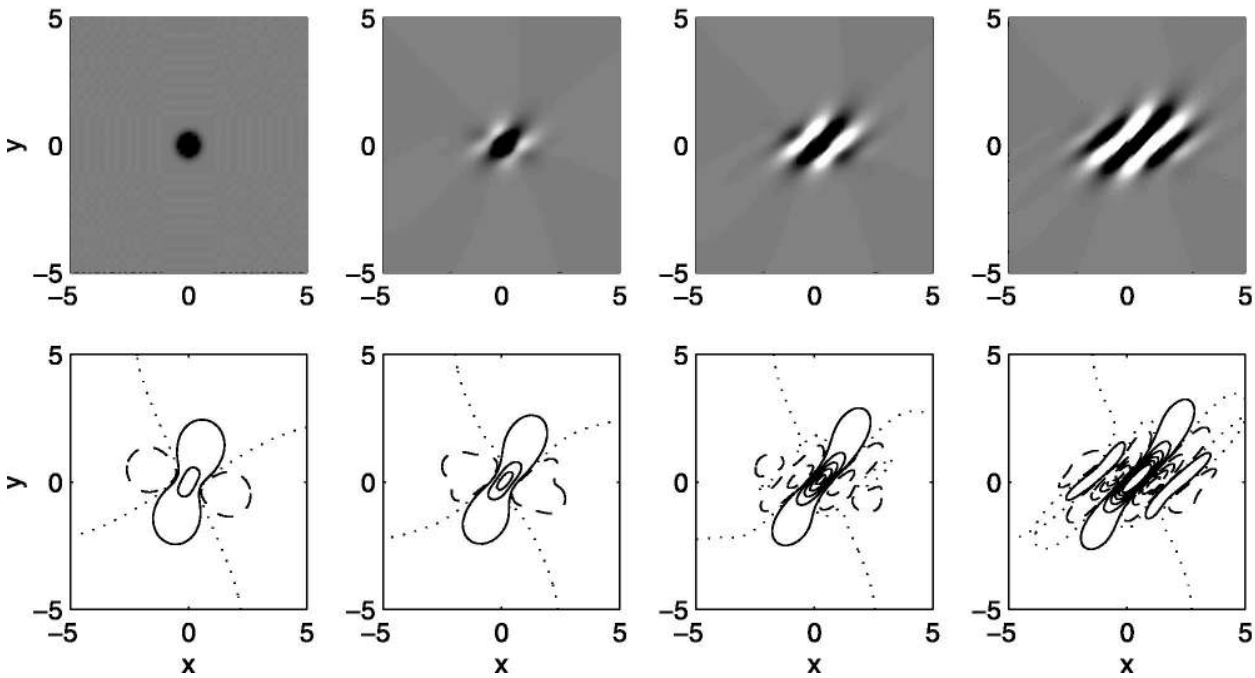

Figure 12. Evolution of a Gaussian sandpit subject to an asymmetric tide in the x direction (highest velocities from left to right) in the case of bed load transport: (top) bed evolution and (bottom) residual currents and from left to right the evaluation times $\tau = 0$, $\tau = 2$, $\tau = 4$, and $\tau = 6$. Troughs are black, crests are white, and the undisturbed seabed is shaded. Solid streamlines correspond to counterclockwise rotation, whereas dashed ones correspond to clockwise rotation. The plotted region covers a dimensional area of about 70×70 km^2. Parameter values are the following: $r = 0.6$, $f = 0.83$, $\beta_b = 3$, and $\lambda = 0.0084$ [*after Roos et al.*, 2001].

a single point may even tempt one into confusing geometrical perceptions. Therefore one should bear in mind that the primary role of the impulse response is that of a tool to be used in the integrated sense according to equations (25) and (40). However, we have seen cases in which most of the qualitative features of the impulse response are retained throughout this integration procedure (e.g., when going from the isolated ridge to the stability analysis in section 3.5 or from the isolated hump to an offshore sandpit in section 6). Apparently, the analytical expression of the impulse response already provides fundamental information on the system's behavior.

[46] Finally, note that the isolated ridge can be seen as an infinite sequence of isolated humps. Hence the one-dimensional impulse can be derived from the two-dimensional one by choosing $z_{b1} = \delta(x)$ in equation (40) (see also the leftmost arrow in Figure 1). Nevertheless, we chose to investigate the isolated ridge separately, as it gives more direct insight into the evolution of y-independent topographies $z_{b1}(x)$.

[47] Despite their limitations, analytical solutions for the flow and bed evolution can be useful for the verification of numerical models. The isolated hump can be implemented easily and, more importantly, does not interfere with the boundaries of a finite numerical domain, as these can be chosen sufficiently far away. The wavy topographies studied in a stability analysis also permit analytical solutions, but the infinite spatial extent of such patterns is likely to cause complications at the boundaries of the numerical domain.

[48] In order to explain the fundamental mechanisms the examples presented here deal mainly with idealized geometries. However, the results also apply to arbitrary topographies (of small amplitude), and the hydrodynamic and morphodynamic response to such a topography can be numerically obtained with the present method. However, alternative numerical methods may be more appropriate for this purpose.

7.2. Model Assumptions and Limitations

[49] By treating the flow in a depth-averaged way, we neglect the vertical flow structure. As such, we are unable to describe the mechanisms related to sand wave formation and dynamics [*Hulscher*, 1996] as these originate from variations in the vertical flow structure. This limits the applicability of the system to the horizontal length scales of sandbanks (on the order of thousands of meters) rather than those of sand waves (hundreds of meters).

[50] The model is linear in the bed amplitude. Consequently, the topographies under consideration should

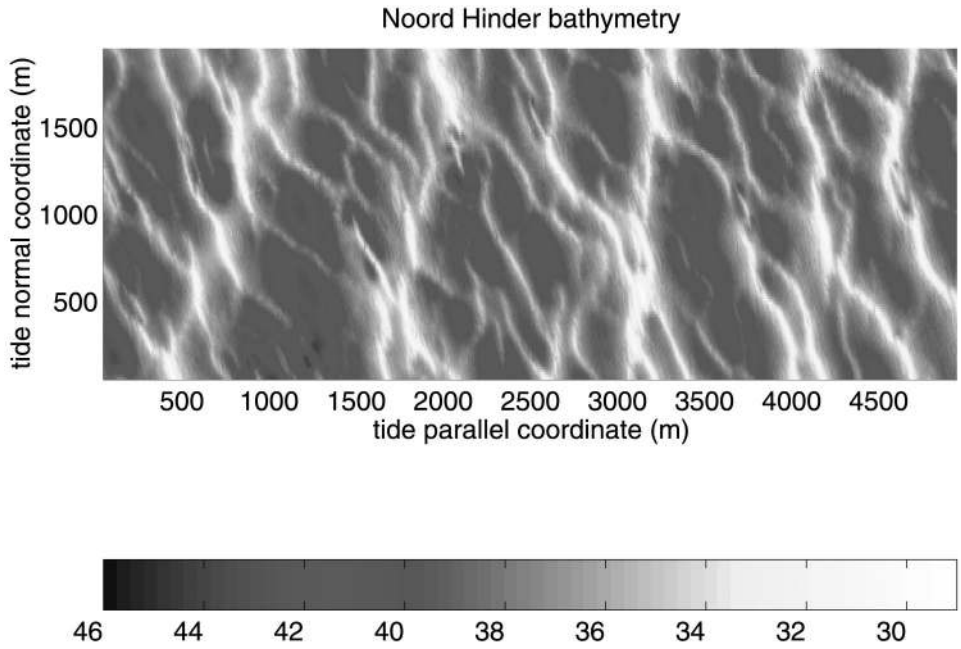

Figure 13. Part of the North Sea bed (area of 10 km^2) [after *Knaapen et al.*, 2001a, Figure 4]. Here the sandbank mode is hardly visible as the smaller-scale sand waves are quite dominant. Figure 13 shows a part of the offshore seabed, large enough to show the topographic variations due to sandbanks and sand waves. The latter mode is not included in two-dimensionally horizontal (2DH) models. The topography on the scales relevant for 2DH models itself is hardly visible, which is not so surprising as nearly one wavelength fits in this figure. Next, the 2DH modeling approach as discussed in this paper predicts a regular pattern of similarly shaped banks (see, e.g., Figure 12). These points illustrate the question in comparing large-scale topographic data with 2DH morphodynamic models: When may we be confident that the data are in agreement with the 2DH morphodynamic model or vice versa? Natural large-scale features as sandbanks always show large irregularities, which may have a stochastic nature or may be due to large-scale nonlinear dynamics. Another problem in performing such comparisons is that the current data sets are not large enough (space), long enough (time), and accurately spaced enough to allow direct comparisons and perform statistics. See color version of this figure at back of this issue.

have small bed amplitudes, compared to the water depth. Nonlinear effects should be taken into account when bed amplitudes are no longer small with respect to the water depth.

[51] The analysis follows a stability concept in which the rigid lid approximation, i.e., neglecting the contribution of z_s^* to the water depth in the model equations, is crucial. Without this assumption an analytical expression for a spatially uniform basic state cannot be found. As Froude numbers are small ($Fr \approx 0.06$), the rigid lid approximation is indeed appropriate. In order to facilitate the analysis we furthermore restrict the basic state to a block flow, and we omit inertial terms in momentum equations.

[52] Furthermore, we neglect wind wave effects, which limits the model's applicability to tide-dominated, thus offshore, conditions. For a detailed description of wave effects in a harmonic stability analysis we refer to *De Vriend* [1990].

7.3. Conclusion

[53] The present analysis shows that the concept of topographic impulse response provides a link between various research subjects within the class of offshore morphodynamic models. A crucial property herein is the inherent instability of the flat seabed, i.e., the tendency of topographic undulations on a flat bed to develop into a pattern of banks, with a preference for cyclonically oriented features. Investigations into the seabed behavior on the corresponding length scales (kilometers) and timescales (decades to centuries) should include the underlying physical mechanisms, such as Coriolis and frictional effects. Furthermore, in predicting the morphodynamic fate of large-scale human intervention, such as navigation dredging and sand extraction, the stability properties should be kept in mind. For instance, modeling a sandpit in either a flat seabed, as carried out in the present study, or in some finite-amplitude equilibrium topography may lead to qualitatively different behavior. To what extent the results will differ strongly depends on the stability properties of such an equilibrium profile as well as on the ratio of pit depth to sandbank height. Furthermore, the model shows that bed load transport can be seen as a limiting case of suspended load transport.

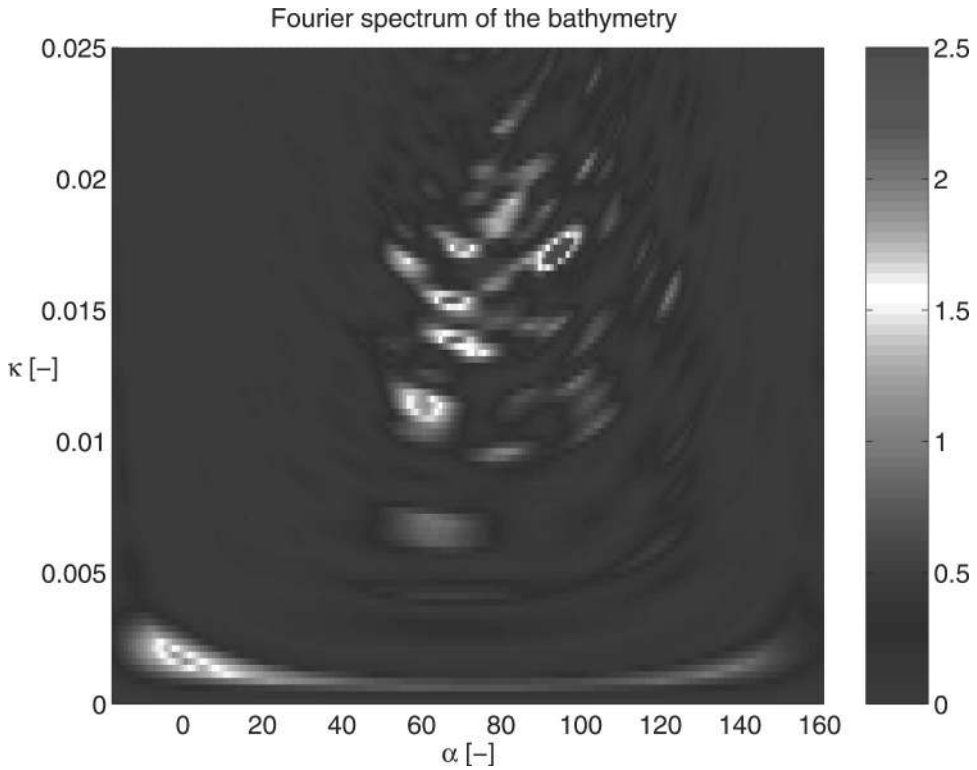

Figure 14. The Fourier transform of the region shown in Figure 13. Herein sandbanks are visible as a relative concentration of energy in the small wave numbers, nearly parallel the principal direction of tidal motion. Besides comparing data with models in the physical domain, one may shift to Fourier space. Figure 14 shows the Fourier transform of Figure 13. Now we observe quite clearly a concentration of energy in the smaller wave numbers, corresponding to the length scale relevant for 2DH models. In this approach the main idea is to find the (mean and deviation) wave number and orientation, which can be converted directly for comparison to the wave vector predicted by the 2DH model; see for example, Figure 6. Besides this the procedure can also be used to filter the smaller-scale features. A more sophisticated way to perform this is using wavelets. See color version of this figure at back of this issue.

7.4. Outlook

[54] Further steps toward a better understanding of large-scale offshore morphodynamics are briefly discussed now. From a modeling point of view a next step is to investigate the morphodynamic model equations (1)–(5) in the nonlinear regime as well. Possible equilibrium topographies then serve as an alternative starting point to model the morphodynamic impact of human intervention.

[55] Accurate data sets, extensive in both space and time, are currently becoming available. In combining with (non)linear models they can be used for validation of the model or processes within the model. *Knaapen et al.* [2001b] showed this for alternate bars, i.e., a large-scale pattern in the fluvial environment. Until now, validation was mostly based on comparing observations with modeled characteristics such as wavelength, etc. We recommend also including comparisons in Fourier space; see, for example, *Knaapen et al.* [2001a] or wavelet methods (Figures 13 and 14). Combining data with nonlinear models may result in locally tuned morphodynamic models as shown by *Knaapen and Hulscher* [2002] for the case of the smaller-scale sandwaves. Data assimilation is not likely to enable a similar study of sandbank dynamics as was carried out for alternate bars [*Knaapen and Hulscher*, 2003], since the data sets are quite limited compared with the morphodynamic timescale. To explore these aspects, a data set comprising more than 100 years of North Sea sandbank observations is currently under investigation.

[56] Sandbanks show irregularities that, so far, deterministic depth-averaged modeling has not reflected. The underlying reasons for observed spatial or temporal variations of amplitudes and wavelengths are not understood, neither from a theoretical nor from an observational point of view. This aspect could be investigated by a cellular automata model, as was done for beach cusps by *Coco et al.* [2001], or by reflecting the stochastic nature of specific parameters (e.g., individual storms, meteorological tide, and sediment properties). A second option is that these deviations from regularity are due to longer-term and/or larger-scale periodicity in hydrodynamic forcing (e.g., variation of the astronomical tide and seasonal or climatological variations). The latter idea is based on the analogy of this morphodynamic system with the coupled atmosphere-ocean system. The

separated scales of dynamics have been shown to result in intermittency, periods of regular behavior separated by periods of chaos [*Van Veen et al.*, 2001; L. Van Veen, Baroclinic flow and the Lorenz-84 model, preprint 1210, Department of Mathematics, University of Utrecht, Utrecht, Netherlands, 2002]. The behavior within these "regular" periods was not necessarily the same. Determining the origin of the irregularities will spawn a better understanding and subsequently a better predictability of the effects of human intervention.

[57] In estuaries and rivers, biology and morphodynamics interact to a large degree. Organisms influence sediment characteristics, and hence seabed morphology, directly and indirectly (e.g., trawler nets ploughing the seabed in chase of bed-resident fish), whereas depth and sediment composition are important habitat parameters for these organisms. It is unknown whether and to what extent biogeomorphology is an issue in the offshore environment. If so, these interactions have to be included for correct modeling of large-scale morphodynamics. Furthermore, the influences of graded sediment on the morphodynamics of offshore features (see, e.g., *Walgreen* [2003] for the case of shoreface-connected ridges or *Blom* [2003] for the case of dunes in rivers) are worth being investigated.

[58] *Komarova and Newell* [2000] have shown that nonlinear interaction between smaller-scale rhythmic features, initiated by vertical flow circulations, might lead to topographic features on the spatial scales of tidal sandbanks. As their two-dimensionally vertical model was limited to one horizontal orientation, the characteristic sandbank orientation could not be verified. Therefore, at the moment, it is unknown to what extent this mechanism interferes with the depth-averaged morphodynamic modeling as reviewed in this paper. We recommend investigating its impact and, if relevant, the possibilities of modeling this mechanism in a simpler way so that it can be incorporated or simulated in two-dimensionally horizontal models.

[59] Gas mining has been shown to be able to cause the formation of tidal sandbanks [*Fluit and Hulscher*, 2002; *Roos and Hulscher*, 2002]. This type of human intervention was modeled as a dish-like depression, subsiding at a constant rate. Other forms of offshore human intervention, large enough to have an impact on sandbank scales, are windmill farms and artificial islands. However, it is yet unclear how the morphodynamic impact of such large-scale intervention can be modeled.

APPENDIX A: DERIVATION OF THE ONE-DIMENSIONAL IMPULSE RESPONSE

[60] The quantities ρ_{b0}, ρ_{b1}, ρ_{b2}, and $\rho_{b3}(x)$ in the bed evolution equation (28) for bed load transport are given by

$$\rho_{b0} = (\beta_b - 1)\langle |I|^{\beta_b} \rangle, \tag{A1}$$

$$\rho_{b1} = \cos\theta[1 + (\beta_b - 1)\cos^2\theta]\langle |I|^{\beta_b - 1} I \rangle, \tag{A2}$$

$$\rho_{b2} = \lambda \langle |I|^{\beta_b} \rangle, \tag{A3}$$

$$\rho_{b3} = \frac{(\beta_b - 1)r}{\cos\theta} \langle |I|^{\beta_b - 1} e^{-rx/(I\cos\theta)} H(Ix) \rangle. \tag{A4}$$

The perturbed concentration is given by

$$c_1 = |I|^{\beta_s - 1} \frac{1 + \beta_s \cos^2\theta}{A \cos\theta} e^{-x/(IA\cos\theta)} H(Ix) + |I|^{\beta_s} \frac{\beta_s P(\theta)}{(1 - Ar)\cos\theta} (e^{-x/(IA\cos\theta)} - e^{-rx/(I\cos\theta)}) H(Ix), \tag{A5}$$

with $P(\theta)$ from equation (30). The quantities ρ_{s0}, $\rho_{s31}(x)$, and $\rho_{s32}(x)$ in the bed evolution equation (31) for suspended load transport are given by

$$\rho_{s0} = \frac{1 + \beta_s \cos^2\theta}{A} \langle |I|^{\beta_s} \rangle, \tag{A6}$$

$$\rho_{s31}(x) = \frac{\beta_s [\langle |I|^{\beta_s} e^{-x/(IA\cos\theta)} H(Ix) \rangle - Ar \langle |I|^{\beta_s} e^{-rx/(I\cos\theta)} H(Ix) \rangle]}{A(1 - Ar)\cos\theta}, \tag{A7}$$

$$\rho_{s32}(x) = \frac{1 + \beta_s \cos^2\theta}{A^2 \cos\theta} \langle |I|^{\beta_s - 1} e^{-x/(IA\cos\theta)} H(Ix) \rangle. \tag{A8}$$

APPENDIX B: DERIVATION OF THE TWO-DIMENSIONAL IMPULSE RESPONSE

[61] Green's function in two dimensions, expressed in terms of the growth rates obtained in section 3.5, reads as follows:

$$G(x, y, \tau) = \int_{-\pi/2}^{\pi/2} \int_{-\infty}^{\infty} e^{\omega(k,\theta)\tau} e^{ik(x\cos\theta + y\sin\theta)} k \, dk \, d\theta + \text{c.c.} \tag{B1}$$

Green's representation theorem in two dimensions is given by [*Gradshteyn and Ryzhik*, 2000]

$$G(\mathbf{x}) = \frac{1}{2\pi} \int\int \nabla^2 G(\boldsymbol{\xi}) \log|\mathbf{x} - \boldsymbol{\xi}| d\boldsymbol{\xi}, \tag{B2}$$

with $\boldsymbol{\xi} = (\xi, \zeta)$. In order to find the frictionally induced stream function ψ_r in equation (43) we follow *Huthnance* [1982b], who employed the transformation $\eta_r = \partial\varphi/\partial y$ and $\psi_r = \partial G/\partial y$. Next, G ensues from Green's representation theorem (60), which, in turn, leads to an expression for ψ_r:

$$\varphi = Ire^{-Irx} H(Ix)\delta(y), \tag{B3}$$

$$G = \frac{-I}{4\pi}\{\log(x^2+y^2) + r \int_{-\infty}^{\infty} H(I\xi)e^{-Ir\xi}\log[(x-\xi)^2+y^2]d\xi\}, \quad \text{(B4)}$$

$$\psi_r = \frac{\partial G}{\partial y} = \frac{-Iy}{2\pi}\left[\frac{1}{x^2+y^2} + r\int_{-\infty}^{\infty}\frac{H(I\xi)e^{-Ir\xi}}{(x-\xi)^2+y^2}\,d\xi\right]. \quad \text{(B5)}$$

The Coriolis-induced contribution can be found by using the transformation $\eta_f = \partial\varphi/\partial x$. Then, the derivation is given by

$$\varphi = -Ife^{-Irx}H(Ix)\delta(y), \quad \text{(B6)}$$

$$\eta_f = \frac{\partial\varphi}{\partial x} = fe^{-Irx}[rH(Ix) - \delta(x)]\delta(y), \quad \text{(B7)}$$

$$\psi_f = \frac{f}{4\pi}[\log(x^2+y^2) - r\int_{-\infty}^{\infty} H(I\xi)e^{-Ir\xi}\log[(x-\xi)^2 + y^2]d\xi]. \quad \text{(B8)}$$

The frictionally induced and Coriolis-induced ISE patterns for steady flow and bed load transport are given by

$$\chi_{br} = \frac{-(\beta_b-1)Ix}{\pi}\left\{\frac{x^2-3y^2}{(x^2+y^2)^3} + r\int_{-\infty}^{\infty} H(I\xi)e^{-Ir\xi}\frac{(x-\xi)^2-3y^2}{[(x-\xi)^2+y^2]^3}\,d\xi\right\}, \quad \text{(B9)}$$

$$\chi_{bf} = \frac{(\beta_b-1)fxy}{\pi}\left\{\frac{1}{(x^2+y^2)^2} - r\int_{-\infty}^{\infty}\frac{H(I\xi)e^{-Ir\xi}}{[(x-\xi)^2+y^2]^2}\,d\xi\right\}, \quad \text{(B10)}$$

respectively. We write the perturbed concentration as the sum of two terms $c_1 = c_\beta + c_A$, for which we find

$$c_\beta = \frac{\beta_s}{A}\left[\int_{-\infty}^{\infty} e^{-\xi/(IA)}\frac{\partial\psi_1}{\partial y}(x-\xi,y)d\xi + H(Ix)e^{-x/(IA)}\delta(y)\right], \quad \text{(B11)}$$

$$\langle c_\beta\rangle = \frac{\beta_s}{2A}\left\{\int_{-\infty}^{\infty} e^{-\xi/A}\left[\frac{\partial\psi_1}{\partial y}(x-\xi,y)\right]_{I=1} - \frac{\partial\psi_1}{\partial y}(x+\xi,y)\Big|_{I=-1}\right]d\xi + e^{-|x|/A}\delta(y)\right\}. \quad \text{(B12)}$$

The derivation of c_A requires an additional transformation $c_A = \partial Q/\partial x$, leading to

$$Q = -AIe^{-Ix/A}H(Ix)\delta(y), \quad \text{(B13)}$$

$$c_A = \frac{\partial Q}{\partial x} = [H(Ix)e^{-Ix/A} - A\delta(x)]\delta(y), \quad \text{(B14)}$$

$$\langle c_A\rangle = \frac{1}{2}e^{-|x|/A}\delta(y) - A\delta(x)\delta(y). \quad \text{(B15)}$$

[62] **ACKNOWLEDGMENTS.** We thank Aart van Harten, Huib de Vriend, and an anonymous reviewer for their comments and Michiel Knaapen for providing Figures 13 and 14. This research was carried out within the EU-project HUMOR, contract number EVK3-CT-2000-00037.

[63] Thomas Torgersen is the Editor responsible for this paper. He thanks four anonymous technical reviewers and one cross-disciplinary reviewer.

REFERENCES

Blom, A., A vertical sorting model for rivers with non-uniform sediment and dunes, Ph.D. thesis, Univ. of Twente, 287 pp., Enschede, Netherlands, 2003.

Blondeaux, P., Mechanics of coastal forms, *Annu. Rev. Fluid Mech.*, *33*, 339–370, 2001.

Calvete, D., H. E. De Swart, and A. Falqués, Effect of depth-dependent wave stirring on the final amplitude of shoreface-connected sand ridges, *Cont. Shelf Res.*, *22*(18–19), 2763–2776, 2002.

Coco, G., D. A. Huntley, and T. J. O'Hare, Regularity and randomness in the formation of beach cusps, *Mar. Geol.*, *178*, 1–9, 2001.

De Vriend, H. J., 2DH mathematical modelling of morphological evolutions in shallow water, *Coastal Eng.*, *11*, 1–27, 1987a.

De Vriend, H. J., Analysis of horizontally two-dimensional morphological evolutions in shallow water, *J. Geophys. Res.*, *92*, 3877–3893, 1987b.

De Vriend, H. J., Inherent stability of depth-integrated mathematical models of coastal morphology, paper presented at IAHR Symposium, Int. Assoc. for Hydraul. Res., Copenhagen, 1988.

De Vriend, H. J., Morphological processes in shallow tidal seas, in *Residual Currents and Long Term Transport*, edited by R. T. Cheng, *Coastal Estuarine Stud.*, vol. *38*, pp. 276–301, Springer-Verlag, New York, 1990.

Dyer, K. R., *Coastal and Estuarine Sediment Dynamics*, John Wiley, New York, 1986.

Dyer, K. R., and D. A. Huntley, The origin, classification and modelling of sand banks and ridges, *Cont. Shelf Res.*, *19*, 1285–1330, 1999.

Fluit, C. C. J. M., and S. J. M. H. Hulscher, Morphological response to a North Sea bed depression induced by gas mining, *J. Geophys. Res.*, *107*(C3), 3022, doi:10.1029/2001JC000851, 2002.

Gradshteyn, I. S., and I. M. Ryzhik, *Table of Integrals, Series and Products*, 6th ed., edited by A., Jeffrey and D. Zwill-

inger, translated from Russian, Academic, San Diego, Calif., 2000.

Hulscher, S. J. M. H., Tidal-induced large-scale regular bed form patterns in a three-dimensional shallow water model, *J. Geophys. Res.*, *101*(C9), 20,727–20,744, 1996.

Hulscher, S. J. M. H., and G. M. Van den Brink, Comparison between predicted and observed sand waves and sand banks in the North Sea, *J. Geophys. Res.*, *106*(C5), 9327–9338, 2001.

Hulscher, S. J. M. H., H. E. De Swart, and H. J. De Vriend, The generation of offshore tidal sand banks and sand waves, *Cont. Shelf Res.*, *13*, 1183–1204, 1993.

Huthnance, J. M., On one mechanism forming linear sand banks, *Estuarine Coastal Shelf Sci.*, *14*, 74–99, 1982a.

Huthnance, J. M., On the formation of sand banks of finite extent, *Estuarine Coastal Shelf Sci.*, *15*, 277–299, 1982b.

Knaapen, M. A. F., and S. J. M. H. Hulscher, Regeneration of sand waves after dredging, *Coastal Eng.*, *46*, 277–289, 2002.

Knaapen, M. A. F., and S. J. M. H. Hulscher, Use of a genetic algorithm to improve predictions of alternate bar dynamics, *Water Resour. Res.*, *39,* doi:10.1029/2002WR001793, in press, 2003.

Knaapen, M. A. F., S. J. M. H. Hulscher, and H. J. De Vriend, A new type of sea bed waves, *Geophys. Res. Lett.*, *28*(7), 1323–1326, 2001a.

Knaapen, M. A. F., S. J. M. H. Hulscher, H. J. De Vriend, and A. Van Harten, Height and wavelength of alternate bars in rivers: Modelling vs. laboratory experiments, *J. Hydraul. Res.*, *39*(2), 147–153, 2001b.

Komarova, N. L., and A. C. Newell, Nonlinear dynamics of sand banks and sand waves, *J. Fluid Mech.*, *415*, 285–312, 2000.

Loder, J. W., Topographic rectification of tidal currents on the sides of Georges Bank, *J. Phys. Oceanogr.*, *10*, 1399–1416, 1980.

Parker, G., Self-formed straight rivers with equilibrium banks and mobile bed. Part 1. The sand-silt river, *J. Fluid Mech.*, *89*, 109–125, 1978.

Pattiaratchi, C., and M. Collins, Mechanisms for linear sandbank formation and maintenance in relation to dynamical oceanographic observations, *Prog. Oceanogr.*, *19*, 117–176, 1987.

Robinson, I. S., Tidally induced residual flows, in *Physical Oceanography of Coastal and Shelf Seas*, edited by B. Johns, pp. 321–356, Elsevier Sci., New York, 1983.

Roos, P. C., and S. J. M. H. Hulscher, Formation of offshore tidal sand banks triggered by a gasmined bed subsidence, *Cont. Shelf Res.*, *22*, 2807–2818, 2002.

Roos, P. C., S. J. M. H. Hulscher, B. G. T. M. Peters, and A. A. Németh, A simple morphodynamic model for sand banks and large-scale sand pits subject to asymmetrical tides, paper presented at Second IAHR Symposium on River, Coastal and Estuarine Morphodynamics, Int. Assoc. for Hydraul. Res., Hokkaido, Japan, 2001.

Talmon, A. M., M. C. L. M. Van Mierlo, and N. Struiksma, Laboratory measurements of the direction of sediment transport on transverse alluvial slopes, *J. Hydraul. Res.*, *33*, 495–517, 1995.

Trowbridge, J. H., A mechanism for the formation and maintenance of shore-oblique sand ridges on storm-dominated shelves, *J. Geophys. Res.*, *100*(C8), 16,071–16,086, 1995.

Van de Kreeke, J., S. E. Hoogewoning, and M. Verlaan, Morphodynamics of a trench in the presence of tidal currents, *Cont. Shelf Res.*, *22*, 1811–1820, 2001.

Van de Meene, J. W. H., *The Shoreface Connected Ridges Along the Central Dutch Coast, Neth. Geogr. Stud.*, vol. 174, Kon. Ned. Aardnjksk. Genoot./Fac. Ruimtelijke Wetensch. Univ. Utrecht, Utrecht, Netherlands, 1994.

Van Rijn, L. C., *Handbook of Sediment Transport by Currents and Waves*, Delft Hydraul., Delft, Netherlands, 1993.

Van Veen, L., T. Opsteegh, and F. Verhulst, Active and passive ocean regimes in a low-order climate model, *Tellus, Ser. A*, *53*, 616–628, 2001.

Walgreen, M., H. E. De Swart, and D. Calvete, Effect of grain size sorting on the formation of shoreface-connected sand ridges, *J. Geophys. Res.*, *108*(C3), 3063, doi:10.1029/2002JC001435, 2003.

Zimmerman, J. T. F., Dynamics, diffusion and geomorphological significance of tidal residual eddies, *Nature*, *290*, 549–555, 1981.

S. J. M. H. Hulscher and P. C. Roos, Water Engineering and Management, University of Twente, P.O. Box 217,7500 AE Enschede, Netherlands. (s.j.m.h.hulscher@utwente.nl; p.c.roos@utwente.nl)

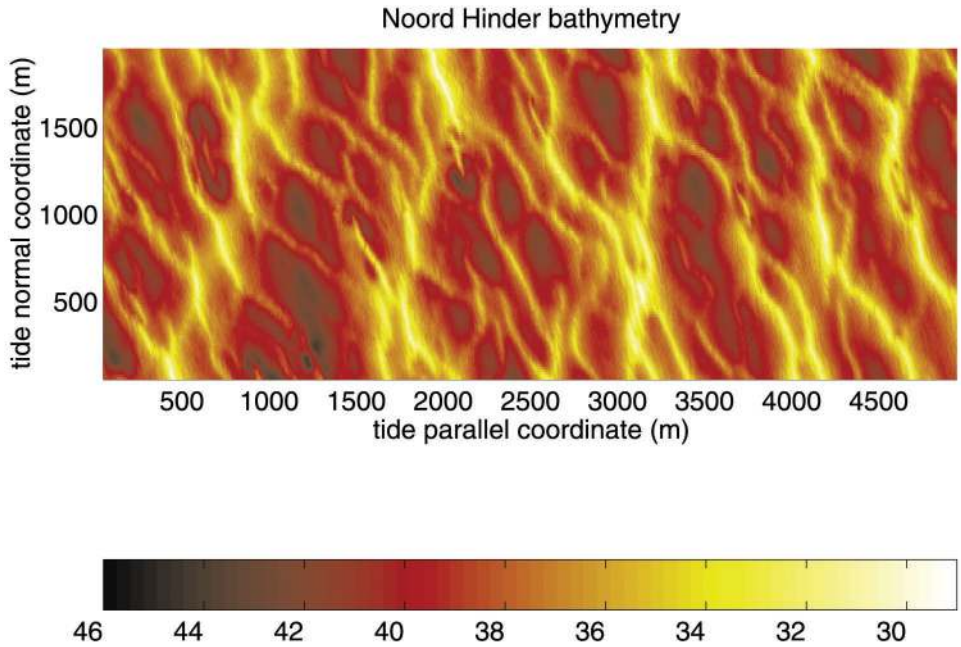

Figure 13. Part of the North Sea bed (area of 10 km^2) [after *Knaapen et al.*, 2001a, Figure 4]. Here the sandbank mode is hardly visible as the smaller-scale sand waves are quite dominant. Figure 13 shows a part of the offshore seabed, large enough to show the topographic variations due to sandbanks and sand waves. The latter mode is not included in two-dimensionally horizontal (2DH) models. The topography on the scales relevant for 2DH models itself is hardly visible, which is not so surprising as nearly one wavelength fits in this figure. Next, the 2DH modeling approach as discussed in this paper predicts a regular pattern of similarly shaped banks (see, e.g., Figure 12). These points illustrate the question in comparing large-scale topographic data with 2DH morphodynamic models: When may we be confident that the data are in agreement with the 2DH morphodynamic model or vice versa? Natural large-scale features as sandbanks always show large irregularities, which may have a stochastic nature or may be due to large-scale nonlinear dynamics. Another problem in performing such comparisons is that the current data sets are not large enough (space), long enough (time), and accurately spaced enough to allow direct comparisons and perform statistics.

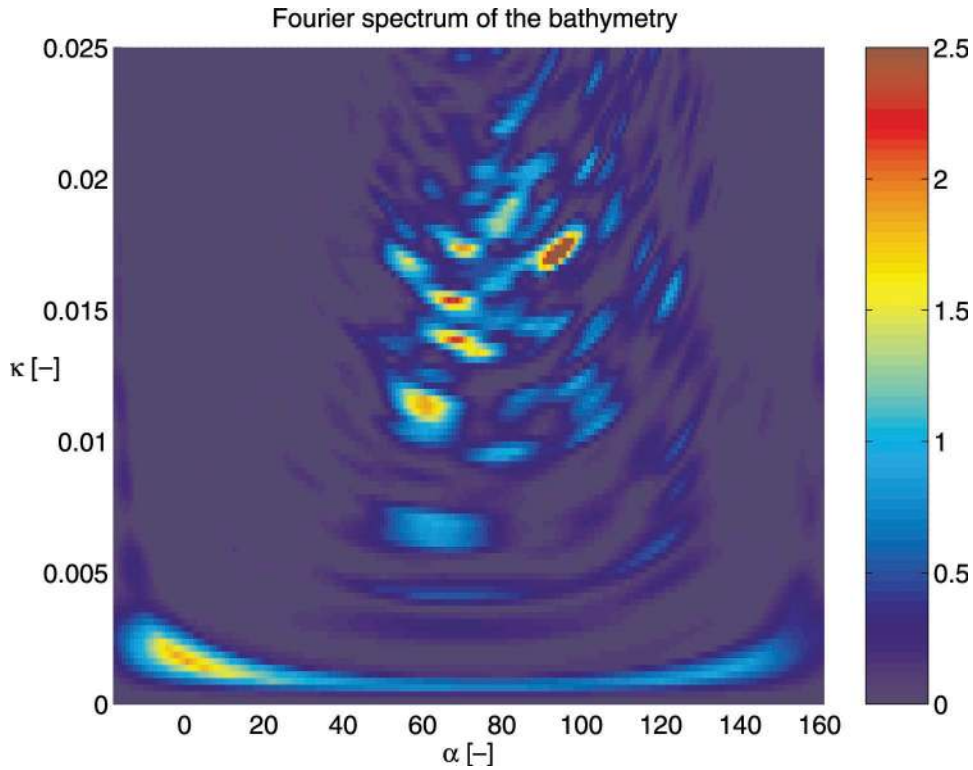

Figure 14. The Fourier transform of the region shown in Figure 13. Herein sandbanks are visible as a relative concentration of energy in the small wave numbers, nearly parallel the principal direction of tidal motion. Besides comparing data with models in the physical domain, one may shift to Fourier space. Figure 14 shows the Fourier transform of Figure 13. Now we observe quite clearly a concentration of energy in the smaller wave numbers, corresponding to the length scale relevant for 2DH models. In this approach the main idea is to find the (mean and deviation) wave number and orientation, which can be converted directly for comparison to the wave vector predicted by the 2DH model; see for example, Figure 6. Besides this the procedure can also be used to filter the smaller-scale features. A more sophisticated way to perform this is using wavelets.